

ORIGINAL ARTICLE

Acid assisted-hydrothermal carbonization of solid waste from essential oils industry: Optimization using *I*-optimal experimental design and removal dye application



Faïçal El Ouadrhiri^{a,*}, Ebraheem Abdu Musad Saleh^b, Kakul Husain^b, Abderrazzak Adachi^a, Anouar Hmamou^a, Ismail Hassan^b, Marwa Mostafa Moharam^{b,c}, Amal Lahkimi^a

^a *Laboratory of Engineering, Molecular Organometallic Materials and Environment, Faculty of Sciences Dhar El Mehraz, Sidi Mohamed Ben Abdellah University, Fez, Morocco*

^b *Chemistry Department, College of Arts & Science, Prince Sattam Bin Abdulaziz University, Wadi Al-Dawaser, Alkharj, Saudi Arabia*

^c *Chemical and Electrochemical Processing Department, Central Metallurgical Research and Development Institute (CMRDI), P.O. Box 87, Helwan 11421, Egypt*

Received 20 December 2022; accepted 26 March 2023

Available online 31 March 2023

KEYWORDS

Solid waste essential oil extraction industry;
Catalytic Hydrothermal carbonization;
I-optimal Design;
Response surface methodology;
Dye Adsorption

Abstract Solid waste (SW) generated from extracting of essential oils from medicinal and aromatic plants (MAPs) is an abundant and renewable resource, but proper recycling is necessary to prevent negative environmental impacts from improper disposal. This study focused on converting SW from essential oil (EO) extraction industry by citric acid-catalyzed hydrothermal carbonization (c-HTC) coupled with chemical activation into a carbonaceous material to remove organic pollutants. For this purpose, an *I*-optimal design coupled with response surface methodology (RSM) was developed to investigate the relationship between the severity factor (SF) of the c-HTC process and citric acid dose (HTC_{cat}) on carbon retention rate (C_{RR}) and hydrochar mass yield (M_Y). Under optimal conditions (5.32 and 2 g for SF and HTC_{cat}, respectively), an optimized hydrochar (HC_{op}) was characterized by a C_{RR} and M_Y of 71.02% and 56.14%, respectively. HC_{op} was chemically activated by KOH solution (AHC_{op}) and characterized by a specific surface area of 989.81 m². g⁻¹, a pore volume of 0.583 cm³. g⁻¹, a higher heating value (HHV) of 37.3 MJ/Kg, oxygenated surface functions such as –OH, –COOH, C–O and a methylene blue (MB) removal rate of 90.71%. In

* Corresponding author.

E-mail address: Faical.elouadrhiri@usmba.ac.ma (F. El Ouadrhiri).

Peer review under responsibility of King Saud University.



Production and hosting by Elsevier

addition, modelling of the adsorption isotherms found that the Freundlich isotherm better describes the experimental data, and the second-order model regulates the adsorption kinetics well. Furthermore, The maximum adsorption capacity of AHC_{op} was 588.24 mg.g^{-1} , with a separation factor of 0.625 under the operating conditions ($t = 6 \text{ h}$, $T = 25 \text{ }^\circ\text{C}$, $m_{(AHC_{op})} = 0.2 \text{ g}$, $[MB]_0 = 300 \text{ mg.L}^{-1}$, and $\text{pH} = 7$), indicating its potential for effectively removing organic pollutants. Together, these results provide crucial information on using c-HTC to convert waste biomass into functional carbon materials to remove organic pollutants efficiently. Therefore, several studies must be conducted out to discover other application fields of this material.

© 2023 The Author(s). Published by Elsevier B.V. on behalf of King Saud University. This is an open access article under the CC BY-NC-ND license (<http://creativecommons.org/licenses/by-nc-nd/4.0/>).

1. Introduction

As the second-richest country in endemic biodiversity in the Mediterranean basin, Morocco has an outstanding floral heritage with more than 4,200 species of plants. With nearly 800 endemic species and 600 species classified as medicinal and aromatic plants (MAPs), Morocco produces approximately 140,000 tons of these plants annually. These plants are the subject of increasing attention due to their use in various areas, including traditional medicine, cosmetics, food preservation, and the extraction of essential oils (EOs) (Ajjoun et al., 2022). The main export products are carob, rosemary, thyme, argan oil, essential oils, and roses. Despite the development of different methods for extracting EOs from MAPs, the ratio between the quantity of EOs produced and the quantity of MAPs processed is very low (mass yield), resulting in significant quantities of extraction by-products (solid waste (SW)) that must be managed. According to (Santana-Méridas et al., 2012), the extraction of 1 kg of EOs from MAPs is estimated to generate 100 kg of solid residue. So, if only in Morocco the production of essential oils reaches 5,000 tons of EOs, mainly destined for Europe and America, it implies the generation of more than 500,000 t/year of solid waste.

Regardless of the method used, the solid residues from extracting EOs are considered waste that must be disposed of directly. However, these residues can be considered valuable raw materials for other waste valorization processes and converted into high-value-added biobased products. In this sense, (Saha and Basak, 2020) reported the different possible routes of valorizing solid biomass residue from the industrial use of MAPs. For example, SW can be used directly as battle feed after the extraction of phytochemicals. However, all these routes seem to be brilliant and promising, but they do not allow for to reduce in the residual biomass volume significantly (Chavan et al., 2018). In addition, the use of solid waste as bio-adsorbent (Agarwal et al., 2020); bio-fuel (Grifoni et al., 2021), soil amendment (Das et al., 2022) or other uses (Slavov et al., 2017) has also been studied.

Generally, the valorization of these solid residues through conventional thermochemical routes such as pyrolysis, gasification, or others poses two major problems: (i) energy efficiency (the need to dry the solid waste before proceeding to pyrolysis) and (ii) environmental impact (the release of greenhouse gases). To overcome these two problems, hydrothermal carbonization (HTC) has emerged as a clean, efficient and low-energy technique for converting solid waste into bio-based carbon materials (El Ouadrhiri et al., 2021; Pavlovič et al., 2013; Titirici and Antonietti, 2010; De et al., 2015; Jain et al., 2016). The HTC technique allows the conversion of any type of biomass or waste (dry and wet) under the effect of temperature [$180 \text{ }^\circ\text{C} - 250 \text{ }^\circ\text{C}$] and vapour saturation pressure in a closed reactor (Okolie, et al., 2022). Despite the many potential benefits of HTC process, its widespread adoption still has significant challenges and limitations, including the need for further research and development to optimize the process and improve its efficiency and cost-effectiveness. It should be noted that several factors can influence the quality of the HTC solid product, namely hydrochar (HC) (Akkaya Saygılı and Saygılı, 2022). However, temperature and reaction time are the most important fac-

tors (Nizamuddin, 2017). Most recently, (Li, 2022) prepared a hydrochar from *Lavandula* straw using the HTC process. Therefore, the authors reported that the optimal condition to obtain a usable hydrochar as combustible was with a severity factor (SF) of 6 with a high importance for the temperature compared to the reaction time.

On the other hand, it is advantageous to use a catalyst in the hydrothermal reaction to improve the HC's physicochemical properties and make the process more profitable (MacDermid-Watts et al., 2020). For example, (Susanti et al., 2019) reported the production of an activated carbon via citric acid-catalyzed HTC (c-HTC) followed by chemical activation by KOH. The resulting activated carbon showed higher specific capacity in the lithium-ion capacitor (LIC) and long-term stability. In addition, (Zhang, 2021) reported the viability of HTC catalyzed by hydrochloric acid and nitric acid for the fabrication of functional microporous hydrochar from *Bamboo* residues. (Hsini et al., 2020) directly used the solid waste from the extraction of EOs from the *Ditrichia* plant as a bio-adsorbent for the removal of Cadmium.

Generally, several wastes and biomasses have been converted into carbonaceous material via c-HTC (Zhang, 2021; Ghaziaskar et al., 2019)– (Xue, 2012; Evcil et al., 2020). However, to the best of our knowledge, no study has been conducted on the valorization of SW from the EOs industry via the c-HTC process. Using SW from the EOs industry to dispose of wastewater pollution after c-HTC treatment could be the best valorization strategy from an economic and environmental perspective.

This study examined the potential to produce a new carbonaceous material using solid waste from the extraction of rosemary (*Rosmarinus officinalis*) plant through the c-HTC process, and its effectiveness in removing organic pollutants from water. Specifically, we investigated: (i) using Response Surface Methodology (RSM), this study aims to develop an optimal experimental design to optimize the mass yield (M_Y) and carbon retention rate (C_{RR}) in hydrochar production through the c-HTC process and to evaluate the impact and presence of interaction between the studied parameters. (ii) The optimized hydrochar was activated through the potassium hydroxide (KOH) impregnation method, and the resulting optimized, and activated hydrochar (AHC_{op}) was characterized. (iii) Assessment of the capacity of AHC_{op} in the adsorption of organic pollutants in wastewater.

The use of solid waste as feedstock for producing of carbonaceous materials has the potential to address environmental issues such as waste management and pollution control. By converting waste into valuable materials through processes like c-HTC and chemical activation, we can address these issues and contribute to developing sustainable and efficient technologies for wastewater treatment.

2. Materials and methods

2.1. Precursor preparation

Solid residues were obtained from extracting EOs from rosemary chosen in this study as carbon precursor. First, the SWs were washed with distilled water (DW), ground in a

GM200 mill (Retsch, GmbH, Germany), and sieved to a particle size fraction of $500 \mu\text{m} < d < 250 \mu\text{m}$ (60–35 mesh) for better decomposition in the c-HTC process, and finally stored in a desiccator for further use.

2.2. Hydrochar and activated hydrochar synthesis

The catalyzed hydrothermal carbonization of SW was carried out in a 100 mL polypropylene-lined (PPL) autoclave. First, 2 g of the SW powder was introduced into the Teflon autoclave with 60 mL of distilled water. Then, according to the experimental design below, citric acid ($\text{C}_6\text{H}_8\text{O}_7$) was added to the mixture as a catalyst for the hydrothermal reaction. Finally, the autoclave was well sealed and heated in an oven at a temperature and time represented by the severity factor. The heating rate was constant ($5 \text{ }^\circ\text{C}/\text{min}$) during the c-HTC process. After natural autoclave cooling, the hydrochar was recovered by centrifugation, washed several times with distilled water and dried in the oven overnight. The optimized hydrochar selected using the above experimental design is named HC_{op} . Furthermore, the obtained HC_{op} was chemically activated by KOH (2 M) solution at $700 \text{ }^\circ\text{C}$ according to the procedure reported in our recent work (El Ouadrhiri et al., 2021). The activated hydrochar is named AHC_{op} .

2.3. Optimal design of experimental

A design of experiment (DoE) is a systematic and scientific approach to evaluating the impact of one or more variables on a specific outcome. The experimental design involves carefully planning and organizing the various elements, including the independent and dependent variables, control conditions, sample size, data collection and analysis methods (Weissman and Anderson, 2015; Ghaedi, 2018). The goal of a DoE is to carefully control and manipulate variables to identify the underlying causes of a specific outcome and optimize processes or products (Antoy, 2014). However, classical DoE does not always address certain issues, such as the need to work with various factors types (Smucker et al., 2018).

The optimal design of experiments is an appropriate tool in practically all situations that suggest the possible use of a flexible experimental design (Goos and Jones, 2011). In fact, rigorous experimental design is required to increase the chances of success in an investigation (Smucker et al., 2018). In general, optimum designs have a flexible structure that allows them to adapt to the limitations imposed by the kind of component and the irregular experimental domain (Pukelsheim, 2006). Moreover, the optimal design with the *I*-criterion, also called the *I*-optimal design, differs from other optimal designs by its ability to give a minor average prediction variance and better estimate the effects of the factors (Ke, 2005). Importantly, *I*-optimality is preferred over other optimization strategies for response surface methodology (RSM) when making a critical prediction (Anderson and Whitcomb, 2014).

In this study, we examined the effect of temperature (HTC_T) and reaction time (HTC_t) combined and catalyst dose (HTC_{Cat}) on two responses, M_Y and C_{RR} . Meanwhile, the severity factor (SF), as calculated using Eq. (1) (Heidari et al., 2019), was introduced to simplify the effect of temperature and reaction time during c-HTC, thus reducing the number of experiments.

$$SF = \log R_0 = \log(t \cdot e^{\frac{(T-100)}{14.75}}) \quad (1)$$

The mathematical equation in Eq. (2) that describes the relationship between the factors (X_i) and responses (Y_i) is a quadratic polynomial, where β_i , β_{ij} , and β_{ii} represent the coefficients for the linear effect, interaction effect, and quadratic effect, respectively, and \mathcal{E}_i represents the error (Goos and Jones, 2011). Using the Design Expert software, an *I*-optimal design was created with ten experiments.

$$Y_i = \beta_0 + \sum_{i=1}^n (\beta_i X_i) + \sum_{i=1}^{n-1} \sum_{j=1}^n (\beta_{ij} X_i X_j) + \sum_{i=1}^n (\beta_{ii} X_i^2) + \mathcal{E}_i \quad (2)$$

Table 1 displays the range of values for the two factors, SF (X_1) and HTC_{Cat} (X_2), in the experiment. However, the SF factor has six levels, calculated to include the effects of HTC_T and HTC_t separately, as shown in Table S1. Additionally, the c-HTC experiments were conducted randomly to mitigate any potential randomized hidden effects. Table 2 presents the experimental matrix of the *I*-optimal design, along with the measured and predicted results for each response. Analysis of variance (ANOVA), lack of fit test and coefficient of determination (R^2), as well as graphical inspection, were used to assess the fit and accuracy of the M_Y and C_{RR} models (Yusop et al., 2021).

In this study, the numerical optimization algorithm was chosen among the various optimization methods because it allows for weight modification and prioritization of the factors and responses (Nocedal and Wright, 2006).

2.4. Characterization of the synthesized materials

Nitrogen physisorption isotherms at 77.35 K were used to investigate the textural characteristics of the HC_{op} and AHC_{op} using an ASAP 2020 manometric analyzer (Micromeritics, USA) (Micromeritics, USA). The specific surface area was calculated by the Brunauer-Emmett-Teller (BET) method in the relative pressure range of 0.05–0.35, and the total pore volume (V_p) was obtained from the amount of nitrogen absorbed at $P/P_0 \approx 0.99$. The micropore volume (V_{micro}) was calculated using the *t*-plot method for the carbon-based materials (ASTM D6556-19) and the mesoporous volume (V_{meso}) was deduced by subtraction. In addition, the pore size distribution (PSD) was determined by the Barrett-Joyner-Halenda (BJH) method (Barrett et al., 1951). The average diameter pores size (D_p) was calculated by assimilating them to a cylindrical shape (Klobes et al., 2006). Fourier Transform Infrared Spectroscopy (FT-IR) was used to identify the functional group of the samples using (Bruker Tensor 27). The morphology of the prepared hydrochars was observed by SEM analysis (scanning electron microscopy) using the JEOL JSM-IT500 InTouch Scope at an accelerating voltage of 16 kV. Crystal phase identification (position and intensity of the diffracted lines) was performed by X-ray diffraction (XRD) using an X-ray diffractometer (PANalytical X'Pert Pro) equipped with Cu-K α radiation (1.54 Å). The samples' point of zero charges (pH_{pzc}) was determined by the pH-drift method, as described in our recent work (El Ouadrhiri et al., 2021).

Carbon (C), hydrogen (H), nitrogen (N), and sulfur (S) elements were all analyzed using an elemental analyzer (2400 CHN Elemental Analyzer, Perkin-Elmer, France), and oxygen

Table 1 Experimental domain of factors in the *I*-optimal design.

Factor	Name	Type	SubType	Coded Low	Coded High	Mean	Std. Dev.
X ₁	HTC _{Cat} (g)	Numeric	Discrete	-1 ↔ 2.00	+1 ↔ 6.00	4.00	1.63
X ₂	SF	Numeric	Discrete	-1 ↔ 4.61	+1 ↔ 5.62	5.06	0.2844

Table 2 *I*-optimal design experimental matrix.

Run	Variables				Responses			
	X ₁ :SF		X ₂ :HTC _{Cat}		M _Y (%)		C _{RR} (%)	
	Natural	Coded	Natural	Coded	Experimental	Predicted	Experimental	Predicted
1	5.32	0.406	2	-1.000	56.57	57.46	69.15	68.89
2	5.05	-0.129	4	0.000	54.87	55.41	67.79	68.11
3	5.05	-0.129	4	0.000	55.79	55.41	68.20	68.11
4	5.32	0.406	6	1.000	48.55	48.76	73.03	72.59
5	5.49	0.743	4	0.000	48.30	47.70	69.65	70.00
6	5.05	-0.129	6	1.000	51.68	51.63	72.02	72.55
7	5.01	-0.208	2	-1.000	65.93	64.68	65.38	65.65
8	4.61	-1.000	2	-1.000	72.80	73.16	59.94	59.94
9	5.05	-0.129	4	0.000	54.98	55.41	68.70	68.11
10	4.61	-1.000	6	1.000	55.55	55.38	70.89	70.80

content was determined by subtracting. Indeed, The higher heat value (HHV) was predicted using the unified model for the torrefied biomass in Eq. (3) reported by (Nhuchhen and Afzal, 2017).

$$HHV = 32,7934 + 0,0053(C)^2 - 0,5321(C) - 2,8769(H) + 0,0608(C) \times (H) - 0,2401(N) \quad (3)$$

In this study, the two responses of interest, M_Y(%) and C_{RR}(%) were introduced to understand the mass and carbon profiles that occur during the c-HTC process. M_Y(%) was calculated using Eq. (4) as reported by (Rodríguez Correa et al., 2018). Therefore, C_{RR}(%) is defined as the ratio of the carbon percentage in the feedstock to the hydrochar (Afolabi et al., 2020) and calculated using Eq. (5).

$$M_Y(\%) = \frac{\text{Mass of dry HC}(g)}{\text{Mass of dry SW}(g)} \times 100 \quad (4)$$

$$C_R(\%) = \frac{\text{amount of carbon in dry HC}}{\text{amount of carbon in dry SW}} = \frac{\%C_{HC}}{\%C_{SW}} \times M_{Y_{HTC}} \times 100 \quad (5)$$

2.5. Adsorption study

Using a UV-visible spectrophotometer, we investigated adsorption capability in the absorption of MB (a basic dye) onto the synthesized samples. For this purpose, 5 mL of the solution was accurately taken at predefined time intervals (15 min), filtered through a membrane filter (0.45 μm), and recorded their absorbance spectrum. The elimination efficiency was calculated using Eq. (6) or the measurement of the concentration as a function of time using Eq. (7), allowing the deter-

mination of the adsorbed quantity (Q_t). NaOH (0.1 M) and HCl (0.1 M) solutions were used to adjust the pH of the solution. However, the experimental results were interpreted using the Langmuir and Freundlich isotherms, and the adsorption kinetics of the pollutants by the prepared carbonaceous materials was studied by the Pseudo-first-order (PSO), pseudo-second-order model (PSO) models and the intra-particle diffusion (IPD) model grouped in Table S2.

$$\text{Removal}\% = \left(1 - \frac{C_t}{C_0}\right) \times 100 \quad (6)$$

$$Q_{e,t} = \frac{(C_0 - C_{e,t}) \times V}{m} \quad (7)$$

3. Results and discussion

3.1. Optimal design of c-HTC process

Generally, the operating conditions of the HTC process, such as SF and the amount of catalyst added in the reaction, directly affect the hydrochar yield. However, results from the *I*-optimal design have been used to develop the mathematical equation between the studied factors and the responses of interest. Statistical modelling of the *I*-optimal design was performed to maximize and examine the interaction effect between the SF and HTC_{cat} factors for each response of interest (M_Y and C_{RR}).

3.1.1. Statistical modeling of M_Y model

Table 3 shows the results of the ANOVA test applied to the M_Y model. The term is statistically significant if the *p*-value < 0.05 (95% confidence). As seen in Table 3, the *p*-val-

ues are < 0.0002 for the full model, indicating that the model is significant. The R^2 value also shows that the M_Y model has an excellent variability of 99.93%. Another statistical measure used to evaluate the model is adequate precision, which gives the signal-to-noise ratio (Politis et al., 2017). It is 32.93% (much higher than 4) in the current work, indicating that the model is suitable for prediction. In addition, the A, B, AB, and A^2 model terms have a p-value < 0.05 and a large F-value of 181.95, 153.39, 23.61, and 12.45, respectively, which shows that these terms have a significant impact on the M_Y . However, the p-value ($= 0.4692$) for the B^2 term was greater than 0.05, showing that this term does not significantly influence the M_Y model. On the other hand, the graphical inspection using the plot of *Predicted vs Actual* values (Fig. 1(a)) shows that all the points are distributed around the diagonal, which confirms that the model is valid for making predictions. In contrast, the *Residuals vs Run* plot (Fig. 1(b)) shows that the points have a random distribution across the set of experiments, which confirms that there is no effect of the order of the experiments on the model (Darvishmotevalli et al., 2019).

Therefore, the final equation regarding the actual factors to predict the M_Y values is presented below (Eq. (8)).

$$M_Y(\%) = 147.77 - 23.78X_1 + 0.88X_2 + 3.2(X_1 \times X_2) + 0.57X_1^2 - 2.96X_2^2 \quad (8)$$

As can be seen from the equation, the catalyst dose added in the hydrothermal reaction has the largest negative effect (-23.78), while the $X_1 \times X_2$ interaction term has the largest positive effect ($+3.2$) on M_Y . In addition, the effect of the two separate factors on the M_Y shown in Fig. 1(c,d) shows that when the severity factor increases from 4.61 to 5.61 the hydrochar mass yield decreases from 62% to 45% for a catalyst dose equal to 4. This means that temperature and time simultaneously influence the hydrochar yield.

The 2D contour (Fig. 1(e)) and 3D (Fig. 1(f)) response surface plots show that there is a wide range of values (the red area) in which the M_Y is optimal.

However, the decrease in M_Y by increasing either the severity factor or the catalyst dose can be explained by the degradation of the components, i.e. cellulose, hemicellulose and lignin of the EOs extraction residues during c-HTC (Rout et al., 2015). A similar trend has also been reported in the literature when HTC of waste from *Lavandin* distillation (Li, 2022) and other waste (Ahring et al., 2015).

3.1.2. Statistical modeling of C_{RR} model

Carbon densification is an interesting property that gives an idea about the efficiency of the HTC process to convert the raw material into a carbon-rich material for energy and environmental applications (Álvarez-Murillo et al., 2015). The ANOVA analysis in Table 4 shows that the quadratic model is statistically significant, with an F-value of 82.04. Additionally, the analysis of the fit statistic shows that the model has good predictive quality, not only by the difference between the adjusted R^2 (0.978) and predicted R^2 (0.899), which is < 0.2 , but also by the F-value of lack of fit (1.87).

The Adeq Precision measurement is a crucial aspect of signal to noise ratio assessment, as it helps to determine the adequacy of the signal with respect to the noise (Sepehrnia et al., 2023). In this research paper, we presented our findings on the interpretation of the result obtained from the Adeq Precision measurement. Our analysis indicated that a ratio greater than 4 is desirable, as it suggests that the signal is strong enough to overcome the noise. This indicates that the signal is adequately strong compared to the noise, making it a positive outcome for the design process. Furthermore, we suggested that the measurement model used in our study can be used as a tool for assessing and improving the quality of a design. However,

Table 3 ANOVA test and fit statistics for the quadratic M_Y model (%).

Source	Sum of Squares	df	Mean Square	F-value	p-value	Remarks
Model	511.13	5	102.23	115.63	0.0002	Significant
X_1 - HTC _{cat}	160.86	1	160.86	181.95	0.0002	
X_2 - SF	135.61	1	135.61	153.39	0.0002	
$X_1 \times X_2$	20.87	1	20.87	23.61	0.0083	
$(X_1)^2$	11.00	1	11.00	12.45	0.0243	
$(X_2)^2$	0.5638	1	0.5638	0.6378	0.4692	
Residual	3.54	4	0.8841			
Lack of Fit	3.03	2	1.52	6.00	0.1428	Not significant
Pure Error	0.5049	2	0.2524			
Total	514.67	9				
R^2						
Adjusted R^2					0.9931	
Predicted R^2					0.9845	
Std. Dev.					0.8638	
Adeq Precision					0.9403	
					34.9542	

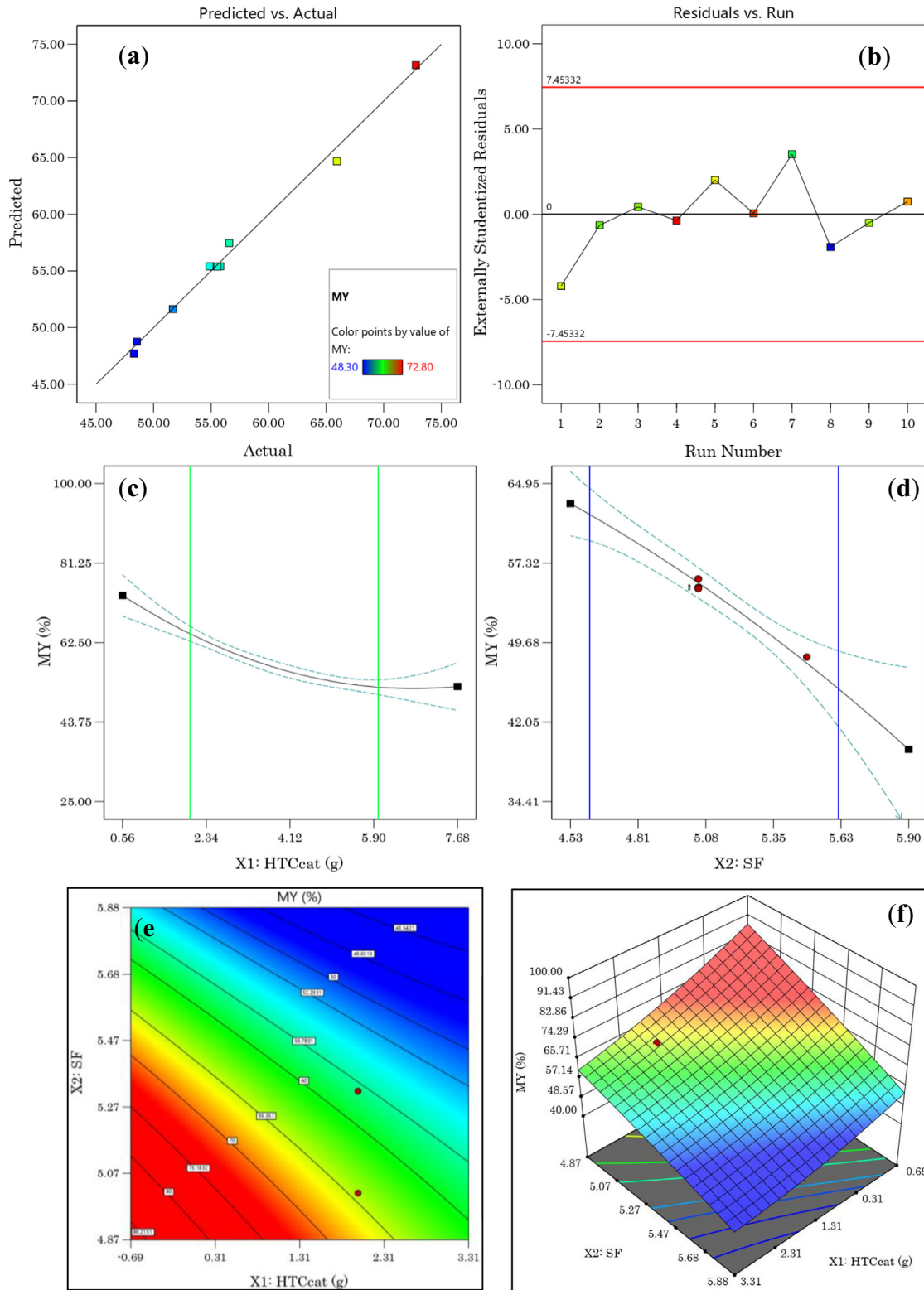


Fig. 1 (a) Predicted vs. Actual value plot, (b) Residuals vs. Run plot, (c) HTC_{cat} effect, (d) SF effect on M_Y , (e) 2D plot, (f) 3D plot response surface of M_Y as a function of SF and HTC_{cat}.

the result of a standard deviation (Std. Dev) of 0.5470 for the C_{RR} model is indicative of a tightly clustered dataset that is relatively close to the fitted curve. Overall, the result of a standard deviation of 0.5470 for the quadratic model is an

important finding that supports the validity of the model and provides important insights into the nature of the data.

In the same context, it is evident that not only the distribution of points around the linear line in the *Predicted vs Actual*

Table 4 ANOVA test and fit statistics for the quadratic C_{RR} model (%).

Source	Sum of Squares	df	Coefficient Estimate	F-value	p-value	Remarks	
Model	122.74	5	24.55	82.04	0.0004	Significant	
X_1 - HTC_{cat}	41.79	1	2.88	139.68	0.0003		
X_2 - SF	17.49	1	3.01	58.45	0.0016		
$X_1 \times X_2$	12.97	1	-2.5	43.34	0.0028		
$(X_1)^2$	3.13	1	-1.22	10.47	0.0318		
$(X_2)^2$	1.84	1	-2.55	6.16	0.0680		
Residual	1.20	4					
Lack of Fit	0.7793	2		1.87	0.3488		Not significant
Pure Error	0.4175	2					
Total	123.93	9					
R^2							
Adjusted R^2		0.9903					
Predicted R^2		0.9783					
Std. Dev.		0.8994					
Adeq Precision		0.5470					
		29.8680					

plot was homogeneous (Fig. 2(a)) but also the residuals of all the experimental points in the *Residuals vs Run* plot are inside the red lines, i.e. it varies only due to common cause variations (Tunç et al., 2020). The model's lack of fit indicates no significant impact of the difference between the actual and predicted values compared to the pure error (Behera et al., 2018). However, according to the p-values in Table 4, the terms X_1 , X_2 , $X_1 \times X_2$, and $(X_1)^2$ are all statistically significant in the C_{RR} model, while HTC_{cat} was the most significant term with an F-value of 139.68. On the other hand, the equation that explains the relationship of C_{RR} as a function of HTC_{cat} and SF (Eq. (9)) shows that both factors and the $(HTC_{cat})^2$ term have a positive impact on the carbon retention rate, while the other terms in the equation have a negative impact.

$$C_{RR}(\%) = -154.47 + 11.88X_1 + 70.80X_2 + -2.52(X_1 \times X_2) + 0.30(X_1)^2 + -5.35(X_2)^2 \quad (9)$$

Indeed, as can be seen in Fig. 2(c), if the catalyst dose (X_1) is increased from 2 g to 6 g, the C_{RR} increases from 65% to 74%. Similarly, in the experimental domain of the severity factor, an increase in the carbon retention rate increased from 59.9% to 71.2% (Fig. 2(d)). On the other hand, the 2D contour and 3D response surface graph shown in Fig. 2(e,f) show two domains (the red-coloured area) where the C_{RR} is optimal. For example, for a citric acid dose and a severity factor of 4.61 and 5.30, respectively, we obtain a hydrochar with a C_{RR} of 70%. Similarly, (Díaz et al., 2010; Heidari et al., 2019; González-Arias, 2020; Li, 2022) have reported results similar to this study.

3.1.3. Numerical optimization of M_Y and C_{RR} model

According to the results obtained from modelling M_Y and C_{RR} response, the severity factor and the citric acid dose play an important role in producing carbonaceous material with high mass yield and carbon retention rate. However, one of the

aspects to be improved in the HTC process is the energy intensity, which makes it more cost-effective and economical (Heidari et al., 2019). Herein, numerical optimization using the desirability function (Amdoun, 2018; El Ouadrhiri et al., 2021) was adopted to determine the optimal mass yield and carbon retention rate level in the hydrochar with the constraints cited in table S3. Out of the seven solutions calculated by the software and represented in Fig. S1, the solution with the highest desirability value (73.9%) was selected as the optimal solution (Fig. 3).

As previously mentioned, this optimization aims to obtain a hydrochar from the solid waste of EOs extraction with optimal carbon content, the highest possible mass yield and the lowest possible energy intensity. On the other hand, under the conditions mentioned in Table S3 and represented in Fig. 3, the carbon retention rate in the optimized hydrochar (HC_{op}) reaches its maximum at 68.7% with an optimal mass yield of 57.99%. Moreover, the experimental validation (Table 5) of the optimal solution ($HTC_{cat} = 2$ g, SF = 5.32) shows only a percentage error of 1.85% and 2.32% for M_Y and C_{RR} , respectively. Consequently, the accuracy of the optimal solution is confirmed.

3.2. Characterization of the HC_{op} and AHC_{op}

The elemental analysis and atomic ratios (O/C) and (H/C) of the raw SW, HC_{op} , and AHC_{op} samples produced under optimal hydrothermal conditions (SF = 5.32 (corresponding to $HTC_T = 210$ °C, $HTC_t = 2$ h) and $HTC_{cat} = 2$ g) are presented in Table 6. As seen in the table (below), the carbon percentages were 67.18% and 81.41% in the HC_{op} and AHC_{op} hydrochars, respectively, representing an increase of 42.24% and 72.37% compared to the raw SW. The increase in carbon content in the activated hydrochar can improve the textural properties and, as a result, their performance in eliminating organic pollutants, according to (Kumar and Jena, 2016).

Meanwhile, the percentage of oxygen was decreased by 38.6% and 70.4% compared to raw SW in HC_{op} and AHC_{op}

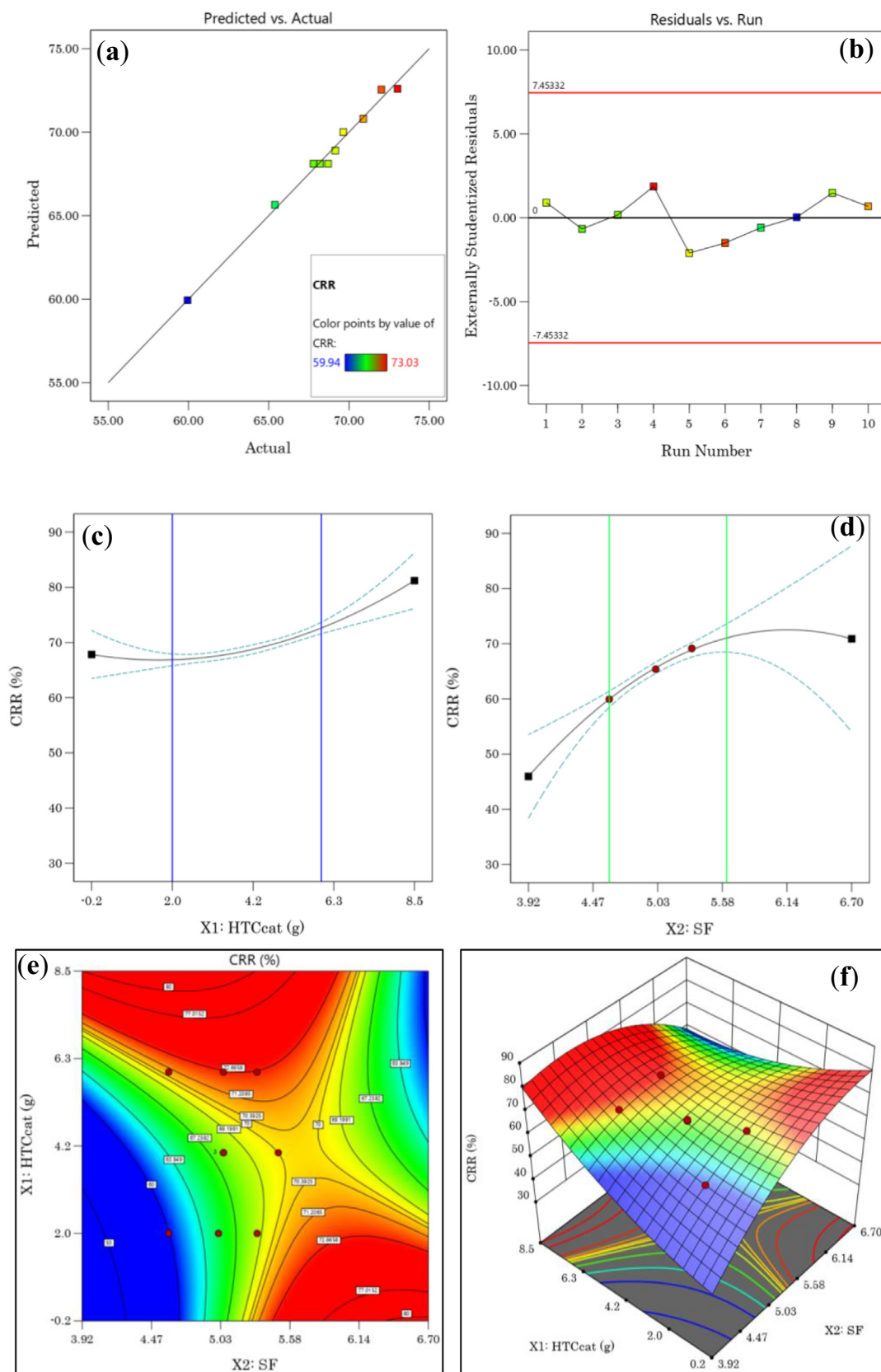


Fig. 2 (a) Predicted vs. Actual plot, (b) Residuals vs. Run plot, (c) HTC_{cat} effect, (d) SF effect on M_Y , (e) 2D plot, (f) 3D plot response surface of C_{RR} as a function of SF and HTC_{cat}.

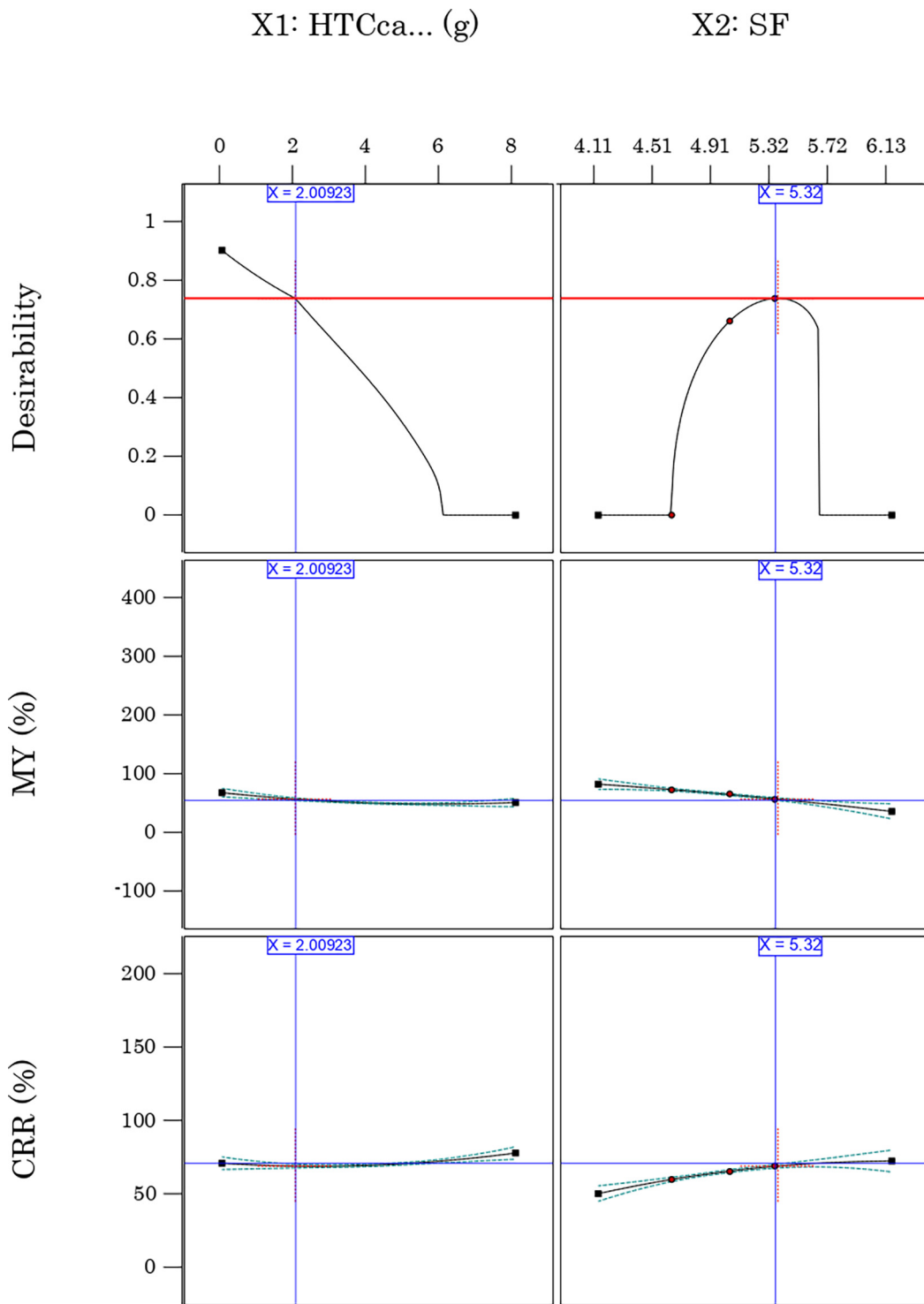


Fig. 3 optimal solution under the imposed constraint.

hydrochars, respectively. This decrease can be explained by the decarboxylation and dehydration reactions that manifest during c-HTC. Interestingly, there is also a significant increase of HHV in the hydrothermal solids HC_{op} (28.29 MJ/Kg) and AHC_{op} (37.30 MJ/Kg) compared to raw SW (19.29 MJ/Kg), which is very interesting from an energy point of view. The

results of the current study are consistent with those of (Román et al., 2012) et (Yao et al., 2016; El Ouadrhiri et al., 2021; Rather et al., 2017). In fact, the increase in HHV and the percentage of carbon retained in hydrochars can be explained by the fact that the organic components containing the lignocellulosic raw SW are partially or completely elimi-

Table 5 Experimental validation of the optimal solution.

HTC _{cat} = 2 g, SF = 5.32 (optimal desirability = 73.9%)			
	Predicted	Experimental	Error
M _Y (%)	57.99	56.14	1.85
C _{RR} (%)	68.7	71.02	2.32

nated during the 210 °C/2h hydrothermal reaction, which is consistent with previous studies (Liu and Balasubramanian, 2012; Akkaya Saygılı and Saygılı, 2022).

The elemental analysis of raw SW was used to calculate the atomic ratio values of O/C and H/C, and the resulting HC_{op} and AHC_{op} hydrochars were plotted in a Van Krevelen diagram (O/C vs H/C) to determine the direction of the hydrothermal reaction. As depicted in Fig. 4, the conversion of raw SW to HC_{op} was primarily driven by the dehydration reaction, which was followed by the decarboxylation reaction. Notably, the AHC_{op} hydrochar was found to be positioned adjacent to bituminous coal in the Van Krevelen diagram, indicating that the c-HTC coupling with KOH activation is a highly effective approach to rapidly generate a carbon-rich material while promoting the hydrolysis of raw SW in a short time.

FT-IR spectrum analysis using pellets of KBr has been performed to evaluate the nature, framework structural characteristics, and surface functionalities attachment to the surface of SW, HC_{op} and AHC_{op} (Fig. 4c). The presence of three intense peaks between 1030 cm⁻¹–1100 cm⁻¹ exhibiting vibrational behaviour can be attributed to the behaviour of carboxylic functional groups (particularly the C-O bond) in the three samples. The wide band located at 3363 cm⁻¹ in the AHC_{op} spectrum compared to the raw SW and HC_{op} spectra could be attributed to the hydroxyl group (–OH). This fact indicates the success of chemical activation with KOH in creating

intense functions at the surface of AHC_{op}. In addition, two very intense peaks between 2925 cm⁻¹ and 2850 cm⁻¹ in the case of AHC_{op} were due to the vibration of the C–H bond. Meanwhile, those located at approximately 1608 cm⁻¹ – 1450 cm⁻¹ and 1710 cm⁻¹ could be attributed to the elongation of the C = C group (aromatic cycles) and C = O, respectively. The presence of the surface functions reported in this work for the activated hydrochar can be explained not only by the effect of the added citric acid in the hydrothermal reaction but also by the operational conditions of the c-HTC process (210 °C, 2 h).

In this study, FTIR analysis showed that adding citric acid in the hydrothermal reaction increased oxygen-containing functional groups (OFGs) in the HC_{op} hydrochar compared to the raw SW. On the other hand, KOH activation further enriched the surface of AHC_{op} with OFGs. Indeed, the findings in terms of peaks and bands found in this study are in line with the observations of (Susanti et al., 2019), who reported a decrease in the intensity of peaks (–OH), (–C–H), and (C–O), when the HTC temperature of *salaca* peel catalyzed by citric acid increased from 200 °C to 250 °C. One of the most important issues that emerge from these results is that OFGs groups serve as an active site that can interact with pollutant molecules, making them crucial for adsorption as reported by (Chen, 2011; An, 2022). In order to collect evidence of crystallinity, the X-Ray diffraction patterns of the powder of raw SW, HC_{op} and AHC_{op} were acquired and presented in Fig. 4 (b). As can be seen, the two characteristic peaks at 2θ = 22.5° and 2θ = 25.23° for AHC_{op} and HC_{op}, respectively, were reflections from the (002) plane of the amorphous carbonaceous structure containing different surface functions. However, the large peak of HC_{op} found compared to AHC_{op} can be explained by the temperature used in the activation step, as reported in other studies (Tu, 2021). However, a peak at 2θ = 44.56° was observed only in the XRD spectrum of AHC_{op}. This peak was characterized from the (100) plane of the graphitic carbon (Gai et al., 2017), indicating the successful

Table 6 Elemental analysis, texturals and physico-chemical properties of SW, HC_{op}, and AHC_{op} samples.

		Samples		
		Raw SW	HC _{op}	AHC _{op}
Elemental analysis	% Carbon	47.23	67.18	81.41
	% Hydrogen	5.3	6.21	5.71
	% Nitrogen	0.69	0.71	0.73
	% Sulfur	0.28	0.18	0.23
	% Oxygen	41.94	25.73	12.4
	HHV (MJ/Kg)	19.29	28.29	37.3
BET	Surface area (m ² .g ⁻¹)	–	68.80	989.81
	Total pores volume (cm ³ .g ⁻¹)	–	0.036	0.583
	Average pores size (nm)	–	20.52	2.36
	Micropore volume (cm ³ .g ⁻¹)	–	0.029	0.535
	Mesopores volume (cm ³ .g ⁻¹)	–	0.007	0.048
Atomic ratio	O/C	0.666	0.287	0.152
	H/C	1.337	1.101	0.908
XRD	Interlayer spacing (d ₀₀₂) (nm)	–	0.388	0.364
	Width height (L _a) (nm)	–	2.50	3.07
	Stacking height (L _c) (nm)	–	1.43	1.59
	Number of layers (N _L)	–	3.68	4.14

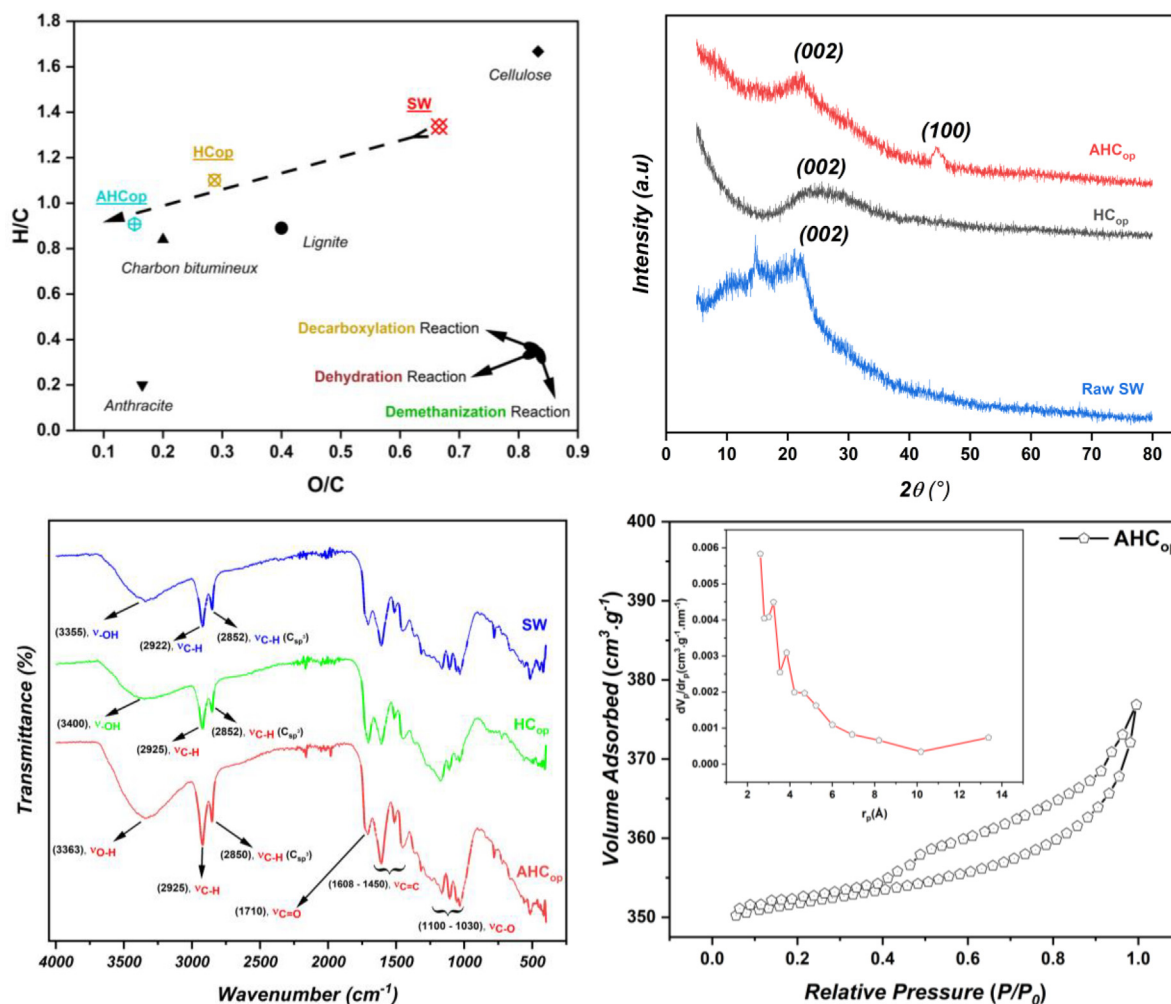


Fig. 4 (a) Van Krevelen diagram, (b) XRD patterns, (c) FTIR spectra of the SW, HCop and AHCop and (d) N₂ adsorption–desorption and PSD profile of AHCop.

preparation of a graphitized carbon material. In fact, the graphitic structure in the AHC_{op} matrix was probably formed in the activation step at 700 °C. In addition, the interlayer spacing (d_{002}) of successive and parallel planes of carbon atoms in the amorphous structure of HC_{op} and AHC_{op} (Table 6) was calculated using Bragg's law ($d_{002} = \frac{\lambda}{2 \times \sin(\theta_{(002)})}$) and found to be 0.388 and 0.364 (high compared to typical graphite layers (0.335 nm)), respectively which indicates an increased crystallinity and graphitization degree. It is essential to point out that the stacking thickness and degree of condensation of the aromatic layers are reflected in the XRD pattern of AHC_{op} by the peaks (002) and (100), respectively. In this sense, specific parameters such as stacking height (L_c), width (L_a), and the number of layers ($N_L = \frac{L_c}{d_{002}}$) are calculated via Bragg's law and Debye-Scherrer's formula ($D = \frac{0.9 \times \lambda}{\beta \times \cos(\theta)}$) (Scherrer, 1918) and processed by fitting method (Huh, 2014) to investigate deeply further the crystal structure modifications of the activated hydrochar AHC_{op} derived from the SW. As shown in Table 6, the d_{002} , L_a , L_c and N increased significantly from HC_{op} to AHC_{op}, indicating that KOH activation at 700 °C increased the degree of graphitization of the activated hydrochar. This result has been described previously in similar studies (Liu,

2020). For carbonaceous adsorbents, adsorption occurs primarily at the interface, and the specific surface area and pore size distribution on the surface of the carbonaceous material are the most important parameters affecting adsorption efficiency (Oginni et al., 2019). The N₂ adsorption profiles and PSD for HC_{op} and AHC_{op} were represented in Fig. S2 and Fig. 4(d), respectively, and the calculated textural parameters were presented in Table 6. The AHC_{op} isotherm may be classified as a type IV(a), characteristic of mesoporous adsorbents and abundant slit-like pores on the surfaces. The presence of a capillary condensation on a desorption branch is indicative of a type H₃ hysteresis loop, as defined by the International Union of Pure and Applied Chemistry (IUPAC) classification (Thommes, 2015). However, the type HC_{op} isotherm is almost the same as that of AHC_{op}, which shows that the KOH activation step at 700 °C does not influence the pore type. The BET-specific surface area and total pore volume of HC_{op} and AHC_{op} are 68.80 m²·g⁻¹ and 0.036 cm³·g⁻¹ and 989.81 m²·g⁻¹ and 0.583 cm³·g⁻¹ respectively, proving the development of porosity in the hydrochar produced by citric acid-assisted HTC followed by the KOH activation step. In fact, as expected, the increase of the BET surface after catalyzed hydrothermal treatment is reported by other studies (Xing

et al., 2019; Susanti et al., 2022). However, the BET surface area of the optimized hydrochar obtained in this study is higher than that reported by (Zhou, 2022) in HTC catalyzed by phosphoric acid. These results can be explained by the nature of the acid catalyst, the type of precursor used and the operating conditions of the HTC process. This fact shows that citric acid is a good candidate for developing high porosity in the hydrochar surface. In addition, the PDS graphs of HC_{op} and AHC_{op} show a pore distribution in the region (2 nm-50 nm), confirming the surface's mesoporous nature with a small number of micropores of 0.029 and 0.535, respectively. SEM analysis was done to show how the c-HTC process and KOH activation affected the morphology of the HC_{op} and AHC_{op} samples. Fig. 5 shows the corresponding images at different magnifications. From a global point of view, the pictures in Fig. 5(a-b) show that the surface of HC_{op} is relatively smooth with less porosity due to the citric acid-assisted hydrothermal treatment. This observation is often reported for other hydrochars derived from lignocellulosic biomass (Liu, 2020; Ghaziaskar et al., 2019; Oumabady et al., 2020; Tu, 2021). Nevertheless, the surface morphology of AHC_{op} presents a quite varied structure and a disorganized texture due to the KOH-activation process at 700 °C. Furthermore, the amorphous carbon regions and graphitic layers are well observed in AHC_{op} with pores on the surface, which are consistent with the amorphous carbon's nature and in agreement with the BET analysis.

Indeed, there are several possible explanations for such a result. First, the penetration of citric acid into the raw SW matrix during the hydrothermal reaction favours better the fragmentation and solubilization reactions of the macromolecules, i.e. cellulose, hemicellulose and lignin in the raw SW, causing profound destruction of the latter (Rodríguez Correa et al., 2018). Then, the activation by KOH significantly increased the porosity and generated more pores in the interior and exterior surfaces of AHC_{op}. Finally, thermal activation at 700 °C left the surface clearer and more graphitic as reported by (Zbair, 2020). Furthermore, the EDS analysis and the AHC_{op} mapping images represented in Fig. 6 indicate the presence of the carbon atom in significant content, with the existence of some impurities such as silica (Si), aluminum (Al), potassium (K) and sulfur (S) in low content. The presence of the chemical elements Si, S and K, detected in EDX, would come from the citric acid and KOH used for the activation, having remained in the AHC_{op} after the washing step. Regarding the element Si, its presence probably comes from the raw SW because it is an inorganic element encountered in the composition of wood ashes and some shells (Tu, 2021). Through the various analysis carried out, it should be noted that the presence of a developed porosity in terms of BET surface and the nature of pores on the surface of AHC_{op}, as well as the presence of oxygenated functional groups, are crucial elements for the application of AHC_{op} in the adsorption of organic pollutants (Dutta et al., 2021).

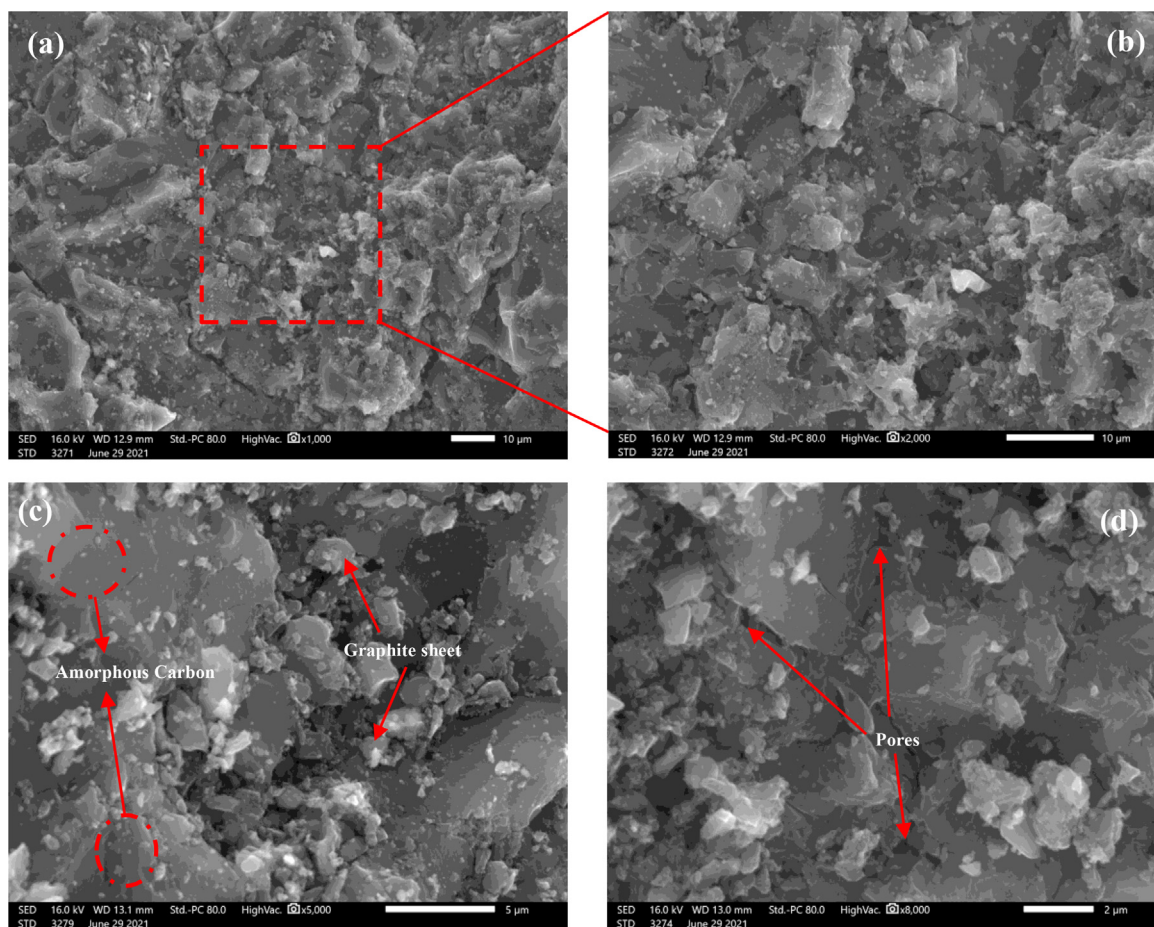


Fig. 5 SEM image at low and high magnification of (a,b) HC_{op}, (c,d) AHC_{op}.

3.3. Adsorption studies

3.3.1. MB Adsorption capacity onto SW, HC_{op} and AHC_{op}

The adsorption capacity of raw SW, HC_{op}, and AHC_{op} on methylene blue, as a pollutant molecule, were investigated and the result are presented in Fig. 7. Their adsorption capacities were 43.54, 134.37, and 340.25 mg.g⁻¹, for raw SW, HC_{op} and AHC_{op}, respectively, under the following conditions: [t = 6 h, V = 250 mL, T = 25 °C, m = 0.2 g, C₀ = 300 mg/L, and pH = 7], corresponding to 11.61%, 35.83%, and 90.73% elimination efficiency. The MB adsorption capacity of AHC_{op} was clearly greater than that of raw SW, and HC_{op} since the citric acid-assisted HTC procedure followed by the KOH-activation stage at 700 °C significantly increased the aromaticity and porosity of AHC_{op}. In addition, the adsorption capacity of HC_{op} was nearly three times that of raw SW, owing to the increase in BET surface area, pore volume, and functional groups of HC_{op} after citric acid-assisted c-HTC, as demonstrated by BET and FT-IR analyses. In contrast, the MB removal rate by AHC_{op} was three times that of HC_{op} under the same circumstances, which is consistent with its large BET surface area (989.81 m².g⁻¹), pore volume, and abundance of OFGs such as -CO, C-H, -C = O, and -OH. Therefore, alkaline activation at 700 °C with KOH is a potential activation technique for enhancing the adsorption performance of activated hydrochar. Subsequently, additional batch experiments were conducted to investigate only MB's adsorption characteristics and kinetics on AHC_{op}.

3.3.2. Adsorption isotherm of AHC_{op}

Langmuir and Freundlich, the two most popular isotherm models for analyzing adsorption capability on AHC_{op}, were

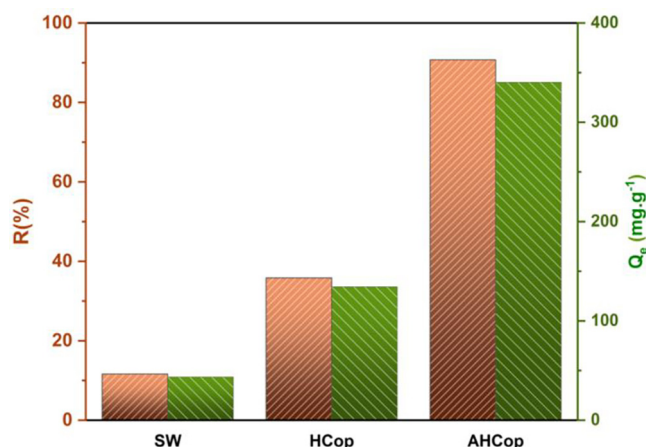


Fig. 7 MB adsorption capacity of raw SW, HC_{op} and AHC_{op}, operating conditions: [t = 6 h, V = 250 mL, T = 25 °C, m = 0.2 g, C₀ = 300 mg.L⁻¹, and pH = 7].

investigated. The Langmuir model explains monolayer adsorption onto an adsorbent surface without interaction between adsorbate molecules (Vinayagam, 2023). In contrast, the Freundlich model predicts multilayer adsorption on an energetically heterogeneous surface with interacting adsorbate molecules (Freundlich, 1907). Fig. 8(a,b) show the plotting of the linear fit curves for the Langmuir and Freundlich isotherm models, respectively, and Table 7 provides the calculated parameters of each of these models. First, the Freundlich model has a slightly higher R² coefficient (0.972) than the Langmuir model (0.967).

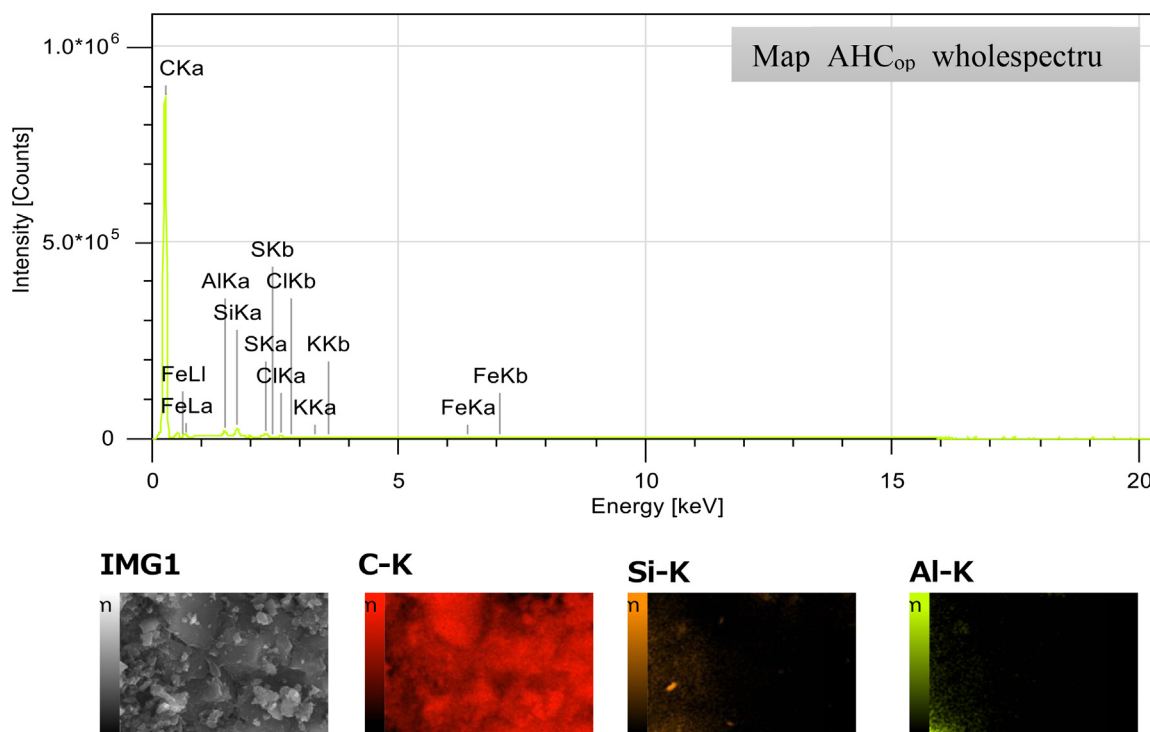


Fig. 6 EDS spectrum and mapping images of AHC_{op}.

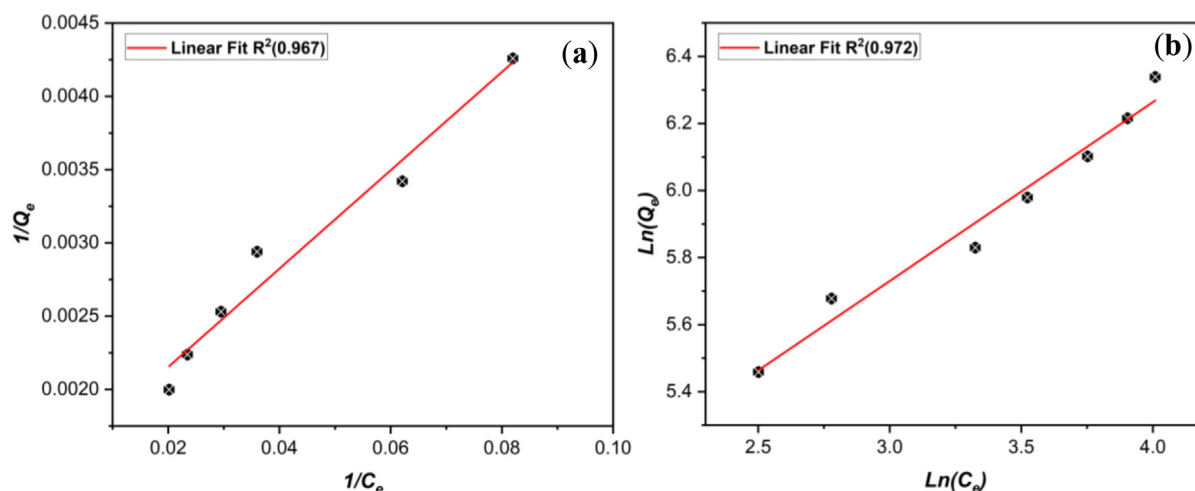


Fig. 8 linear fit curves for the (a) Langmuir and (b) Freundlich isotherm models.

These results suggest that both models describe the adsorption process of MB on AHC_{op} , indicating that the adsorption occurs in a monolayer way on a homogeneous surface and in a multi-layer way on a heterogeneous surface (Kurnia, 2022). Furthermore, the Freundlich constant ($1/n_F$) equals 0.534 between 0 and 1, indicating intensive adsorption between the MB molecules and the AHC_{op} . In addition, the calculation of the separation factor (R_L) ($R_L = \frac{1}{1+K_L \cdot C_0}$) (Veloso et al., 2020), obtained from the Langmuir model, resulted in a value of 0.625, which was substantially below 1, which indicates that the adsorption of MB molecules on AHC_{op} is thermodynamically advantageous and thus a sign of a high affinity of AHC_{op} towards MB molecules (Theydan and Ahmed, 2012).

This result can be expressed by the large specific surface area that AHC_{op} possesses and the richness of the surface by OFGs that contribute positively to the adsorption process (Supong et al., 2022). In addition, the point of zero charges (pH_{zhc}) was measured and represented in Fig. 9(b). As can be seen, AHC_{op} has a pH_{zhc} of 6.40, which means that at pH values below 6.40, the surface of AHC_{op} is positively charged, facilitating the adsorption of negatively charged molecules. On the other hand, at a pH above 6.40, the surface is negatively charged, facilitating the adsorption of basic dyes (Kurnia, 2022). The removal efficiency of MB at $pH = 7$ can be explained by the fact that the surface of AHC_{op} has been negatively charged, which increases the adsorption of the negatively charged MB molecules at $pH = 7$.

3.3.3. Adsorption kinetic of AHC_{op}

Adsorption kinetics models are mathematical equations that describe the rate at which a substance, known as the adsorbate, is adsorbed onto the surface of a solid or liquid, known as the adsorbent. These models are used to predict and understand the behaviour of adsorption processes and can be used to design and optimize adsorption systems. Two of the most widely used adsorption kinetics models are the pseudo-first-order model (PFO) and the pseudo-second-order model (PSO) (Benjelloun et al., 2021). Table 8 shows the experimental capacity of MB adsorption onto AHC_{op} , and the associated calculated parameters of PSO and PFO, and Fig. 9(c,d) shows the graphs of these models.

Fig. 9(a) shows that the adsorption process can be divided into three stages. In the first stage, the adsorption capacity of AHC_{op} rapidly increases and reaches 150 mg.g^{-1} within 30 min. An exponential increase in the second stage results in a capacity of 291.75 mg.g^{-1} after 250 min. In the third stage, the capacity approaches a stable equilibrium, reaching a maximum of 340.25 mg.g^{-1} after an additional 350 min. On the other hand, the high R^2 values (0.98) show that the PSO kinetics were a good fit for the MB adsorption on AHC_{op} data over the whole adsorption period. Indeed, the theoretical $Q_{e, cal}$ values agreed well with the experimental $Q_{e, exp}$ values, suggesting that chemisorption predominated in the adsorption of MB by AHC_{op} (Agboola and Benson, 2021; Elsayed et al., 2022).

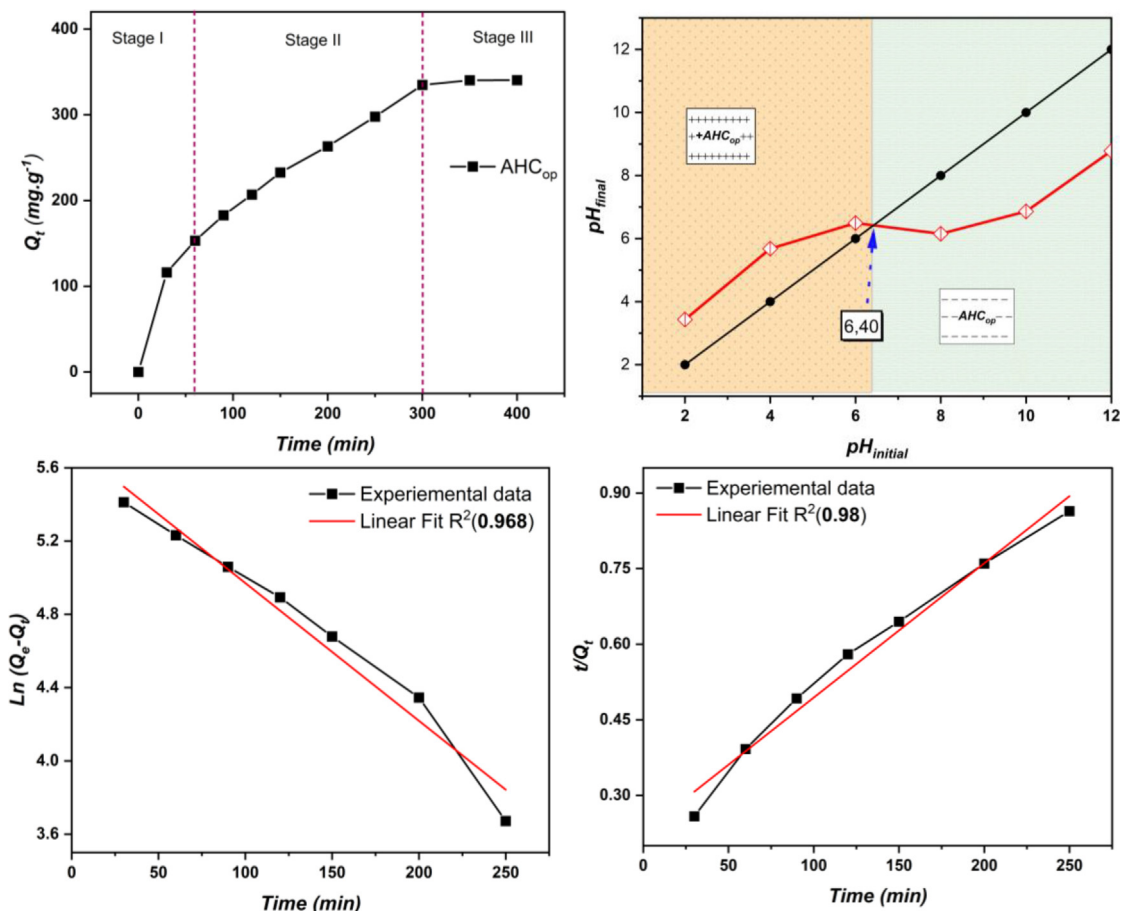
The intra-particle diffusion model has frequently been used to analyze organic contaminants' adsorption on solid surfaces (Salah omer et al., 2022). It has been proven to describe the adsorption process (McKay et al., 1987). It is based on the idea that the adsorption rate is limited by the rate at which the pollutant molecules can diffuse through the pores of the solid material (Sekine and Nakatani, 2002). The IPD model was developed by Weber and Morris using the following equation: $Q_t = K_{IPD} \cdot t^{0.5} + c$ to describe the mass transfer process (Masinga et al., 2022).

As seen in Table 9, the IPD model has a higher R^2 (0.916), which means that the external mass transfer contributes significantly to the process of MB adsorption by AHC_{op} because the linear part intercepts of the plots are significant.

Indeed, two linear parts were seen in the plot of Q_t versus $t^{0.5}$, shown in Fig. 10. The first part can be attributed to the MB molecules transfer through the liquid film to the outer surface of the AHC_{op} , known as the film diffusion (Yao and Chen, 2017). The second part can be attributed to the transport of MB molecules from the AHC_{op} exterior surface to the pores or capillaries of the adsorbent internal structure, known as intraparticle diffusion (Kurnia, 2022). In fact, numerous investigations have revealed non-zero intercepts, showing that the rate-limiting phase in most adsorption processes includes intra-particle and film diffusion (Hameed and El-Khaiary, 2008; Doke and Khan, 2017; Vadivelan and Vasanth Kumar, 2005; Kurnia, 2022; Lopes, 2021). On the other hand, the significant value of the constant C was

Table 7 Langmuir and Freundlich isotherm parameter for MB adsorption onto AHC_{op}.

R _L	Langmuir			Freundlich		
	Q _m (mg/g)	K _L (L/mg)	R ²	K _F (mg/g.(1/mg))	1/n _F	R ²
0.625	588.24	0.002	0.967	61.56	0.534	0.980

**Fig. 9** (a) adsorption capacity of MB on AHC_{op} as a function of time, (b) Point of zero charge of AHC_{op}, linear fitting of (c) PFO model and (d) PSO model.**Table 8** PFO and PSO kinetic parameter for MB adsorption onto AHC_{op}.

model	PFO				PSO		
parameter	Q _{e, exp} (mg.g ⁻¹)	Q _{e, cal} (mg.g ⁻¹)	k ₁ (min ⁻¹)	R ²	Q _{e, cal} (g/mg/min)	k ₂	R ²
AHC _{op}	340.25	314.66	0.0073	0.968	384.61	2.9 × 10 ⁻⁵	0.98

67.7 mg.g⁻¹, which is very far from zero, indicating that the boundary layer is thicker (Magdy and Altaher, 2018).

To determine the efficiency of the prepared AHC_{op} compared to other low-cost adsorbents, the maximum adsorption capacity (Q_m) values were compared. As shown in Table S4, the prepared AHC_{op} activated with KOH had a comparable adsorption capacity for MB to other low-cost adsorbents. Based on this comparison, the prepared AHC_{op} from the solid waste-based essential oil industry is a promising and effective option for removing MB from aqueous solutions due to its rel-

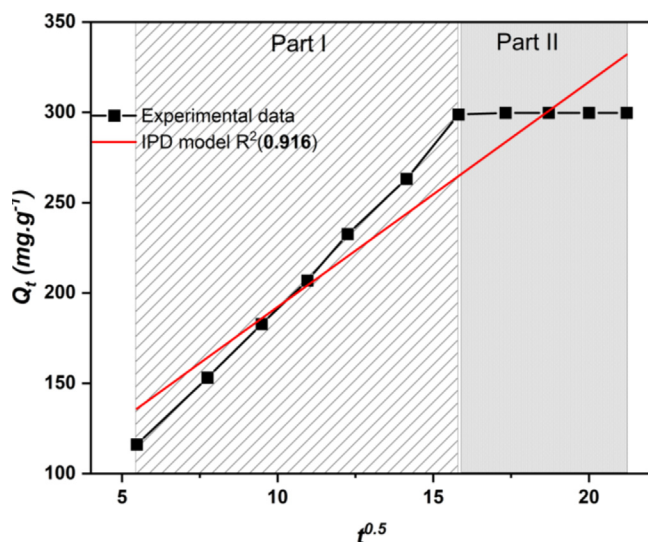
atively high adsorption capacity. However, studying the regeneration of the material after its use would support the results obtained and further enrich the discussion.

4. Conclusion

In conclusion, the *I*-optimal experimental design proved to be an effective method for examining the relationship between the factors and responses studied in this work. By optimizing the hydrochar production conditions, the HC_{op} obtained displayed high M_Y(%) and

Table 9 Parameters of the IPD model for MB adsorption onto AHC_{op}.

Model	Intra-Particule Diffusion		
Parameter	K _{IPD} (mg/g/min ^{0.5})	C (mg/g)	R ²
AHC _{op}	12.46	67.7	0.916

**Fig. 10** Intra-particle diffusion model for MB adsorption onto AHC_{op}.

C_{RR}(%) values, making it a promising material for further activation. The KOH (2 M) chemical activation of HC_{op} at 700 °C provides an activated hydrochar (AHC_{op}) with a high specific surface area, amorphous and graphitized structure, and dominance of mesopores as confirmed by SEM-EDS, XRD, and BET analysis. The adsorption experiments conducted on AHC_{op} showed a high maximum adsorption capacity for MB and demonstrated the suitability of the Freundlich, Langmuir, and pseudo-second-order kinetics and intra-particle diffusion models for describing the isotherm and adsorption kinetics. Overall, this study has successfully developed and characterized a promising activated hydrochar for removing of MB from wastewater.

CRediT authorship contribution statement

Faiçal El Ouadrhiri: Conceptualization, Methodology, Software, Validation, Formal analysis, Investigation, Resources, Data curation, Writing – original draft, Writing – review & editing, Visualization. **Ebraheem Abdu Musad Saleh:** Methodology, Validation, Investigation, Resources, Writing – review & editing, Project administration, Funding acquisition. **Kakul Husain:** Resources, Writing – review & editing. **Abderrazzak Adachi:** Conceptualization, Investigation, Resources, Data curation. **Anouar Hmamou:** Conceptualization. **Ismail Hassan:** Resources. **Marwa Mostafa Moharam:** Validation, Funding acquisition. **Amal Lakhimi:** Conceptualization, Writing – review & editing, Supervision, Project administration, Funding acquisition.

Data Availability Statement:

Not applicable.

Declaration of Competing Interest

The authors declare that they have no known competing financial interests or personal relationships that could have appeared to influence the work reported in this paper.

Acknowledgements

We would like to express our sincere gratitude to the Prince Sattam Bin Abdulaziz University for their collaboration on this project. Their support were invaluable in helping us to achieve our research goals. We are grateful for the opportunity to work with such a distinguished institution.

Appendix A. Supplementary data

Supplementary data to this article can be found online at <https://doi.org/10.1016/j.arabjc.2023.104872>.

References

- “ASTM D6556-19, Standard Test Method for Carbon Black-Total and External Surface Area by Nitrogen Adsorption,” ASTM International, West Conshohocken, PA, 2014.
- Afolabi, O.O.D., Sohail, M., Cheng, Y.L., 2020. Optimisation and characterisation of hydrochar production from spent coffee grounds by hydrothermal carbonisation. *Renew. Energy* 147, 1380–1391. <https://doi.org/10.1016/j.renene.2019.09.098>.
- A. Agarwal, U. Upadhyay, I. Sreedhar, S. A. Singh, and C. M. Patel, “A review on valorization of biomass in heavy metal removal from wastewater,” *Journal of Water Process Engineering*, vol. 38. Elsevier, p. 101602, Dec. 01, 2020. doi: 10.1016/j.jwpe.2020.101602.
- O. D. Agboola and N. U. Benson, “Physisorption and Chemisorption Mechanisms Influencing Micro (Nano) Plastics-Organic Chemical Contaminants Interactions: A Review,” *Frontiers in Environmental Science*, vol. 9. Frontiers Media S.A., p. 167, May 28, 2021. doi: 10.3389/fenvs.2021.678574.
- Ahring, B.K., Biswas, R., Ahamed, A., Teller, P.J., Uellendahl, H., 2015. Making lignin accessible for anaerobic digestion by wet-explosion pretreatment. *Bioresour. Technol.* 175, 182–188. <https://doi.org/10.1016/j.biortech.2014.10.082>.
- M. Ajjoun, L. Kharchoufa, I. Alami Merrouni, and M. Elachouri, “Moroccan medicinal plants traditionally used for the treatment of skin diseases: From ethnobotany to clinical trials,” *Journal of Ethnopharmacology*, vol. 297. Elsevier, p. 115532, Oct. 28, 2022. doi: 10.1016/j.jep.2022.115532.
- Akkaya Saygılı, G., Saygılı, H., 2022. Hydrothermal conversion of lignocellulosic waste to value-added biomaterial for high-performance contaminant removal: focusing on synthesis route and uptake mechanism. *Mater. Chem. Phys.* 286,. <https://doi.org/10.1016/j.matchemphys.2022.126219> 126219.
- Álvarez-Murillo, A., Ledesma, B., Román, S., Sabio, E., Gañán, J., 2015. Biomass pyrolysis toward hydrocarbonization. influence on subsequent steam gasification processes. *J. Anal. Appl. Pyrolysis* 113, 380–389. <https://doi.org/10.1016/j.jaap.2015.02.030>.
- Amdoun, R. et al, 2018. The desirability optimization methodology; a tool to predict two antagonist responses in biotechnological systems: case of biomass growth and hyoscyamine content in elicited *Datura starmonium* hairy roots. *Iran. J. Biotechnol.* 16 (1), 11–19. <https://doi.org/10.21859/ijb.1339>.

- An, Q. et al, 2022. Resource utilization of agricultural waste: converting peanut shell into an efficient catalyst in persulfate activation for degradation of organic pollutant. *Chemosphere* 304., <https://doi.org/10.1016/j.chemosphere.2022.135308> 135308.
- Anderson, M.J., Whitcomb, P.J., 2014. Practical aspects for designing statistically optimal experiments. *J. Stat. Sci. Appl.* 2 (3), 85–92. <https://doi.org/10.17265/2328-224x/2014.03.001>.
- J. Antoy, *Design of Experiments for Engineers and Scientists: Second Edition*. Elsevier Ltd, 2014. doi: 10.1016/C2012-0-03558-2.
- Barrett, E.P., Joyner, L.G., Halenda, P.P., 1951. The determination of pore volume and area distributions in porous substances. I. computations from nitrogen isotherms. *J. Am. Chem. Soc.* 73 (1), 373–380. <https://doi.org/10.1021/ja01145a126>.
- Behera, S.K., Meena, H., Chakraborty, S., Meikap, B.C., 2018. Application of response surface methodology (RSM) for optimization of leaching parameters for ash reduction from low-grade coal. *Int. J. Min. Sci. Technol.* 28 (4), 621–629. <https://doi.org/10.1016/j.ijmst.2018.04.014>.
- M. Benjelloun, Y. Miyah, G. Akdemir Evrendilek, F. Zerrouq, and S. Lairini, “Recent Advances in Adsorption Kinetic Models: Their Application to Dye Types,” *Arabian Journal of Chemistry*, vol. 14, no. 4. Elsevier, p. 103031, Apr. 01, 2021. doi: 10.1016/j.arabjc.2021.103031.
- P. Chavan, A. K. Singh, and G. Kaur, “Recent progress in the utilization of industrial waste and by-products of citrus fruits: A review,” *Journal of Food Process Engineering*, vol. 41, no. 8. John Wiley & Sons, Ltd, p. e12895, Dec. 01, 2018. doi: 10.1111/jfpe.12895.
- Chen, Z. et al, 2011. Simple approach to carboxyl-rich materials through low-temperature heat treatment of hydrothermal carbon in air. *Appl. Surf. Sci.* 257 (20), 8686–8691. <https://doi.org/10.1016/j.apsusc.2011.05.048>.
- Darvishmotevalli, M., Zarei, A., Moradnia, M., Noorisepehr, M., Mohammadi, H., 2019. Optimization of saline wastewater treatment using electrochemical oxidation process: Prediction by RSM method. *MethodsX* 6, 1101–1113. <https://doi.org/10.1016/j.mex.2019.03.015>.
- S. K. Das, G. K. Ghosh, and R. Avasthe, “Valorizing biomass to engineered biochar and its impact on soil, plant, water, and microbial dynamics: a review,” *Biomass Conversion and Biorefinery*, vol. 12, no. 9. Springer, pp. 4183–4199, Jun. 30, 2022. doi: 10.1007/s13399-020-00836-5.
- De, S., Balu, A.M., Van Der Waal, J.C., Luque, R., 2015. Biomass-derived porous carbon materials: synthesis and catalytic applications. *ChemCatChem* 7 (11), 1608–1629. <https://doi.org/10.1002/cctc.201500081>.
- Diaz, M.J., Cara, C., Ruiz, E., Romero, I., Moya, M., Castro, E., 2010. Hydrothermal pre-treatment of rapeseed straw. *Bioresour. Technol.* 101 (7), 2428–2435. <https://doi.org/10.1016/j.biortech.2009.10.085>.
- Doke, K.M., Khan, E.M., 2017. Equilibrium, kinetic and diffusion mechanism of Cr(VI) adsorption onto activated carbon derived from wood apple shell. *Arab. J. Chem.* 10, S252–S260. <https://doi.org/10.1016/j.arabjc.2012.07.031>.
- S. Dutta, B. Gupta, S. K. Srivastava, and A. K. Gupta, “Recent advances on the removal of dyes from wastewater using various adsorbents: A critical review,” *Materials Advances*, vol. 2, no. 14. Royal Society of Chemistry, pp. 4497–4531, Jul. 21, 2021. doi: 10.1039/d1ma00354b.
- El Ouadrhiri, F., Elyemni, M., Lahkimi, A., Lhassani, A., Chaouch, M., Taleb, M., 2021. Mesoporous carbon from optimized date stone hydrochar by catalytic hydrothermal carbonization using response surface methodology: application to dyes adsorption. *Int. J. Chem. Eng.* 2021, 5555406. <https://doi.org/10.1155/2021/5555406>.
- Elsayed, I., Madduri, S., El-Giar, E.M., Hassan, E.B., 2022. Effective removal of anionic dyes from aqueous solutions by novel polyethylenimine-ozone oxidized hydrochar (PEI-OzHC) adsorbent. *Arab. J. Chem.* 15, (5). <https://doi.org/10.1016/j.arabjc.2022.103757> 103757.
- Evcil, T., Simsir, H., Ucar, S., Tekin, K., Karagoz, S., 2020. Hydrothermal carbonization of lignocellulosic biomass and effects of combined Lewis and Brønsted acid catalysts. *Fuel* 279., <https://doi.org/10.1016/j.fuel.2020.118458> 118458.
- Freundlich, H., 1907. Über die adsorption in Lösungen. *Zeitschrift Phys. Chem.* 57U (1), 385–470. <https://doi.org/10.1515/zpch-1907-5723>.
- Gai, C., Zhang, F., Lang, Q., Liu, T., Peng, N., Liu, Z., 2017. Facile one-pot synthesis of iron nanoparticles immobilized into the porous hydrochar for catalytic decomposition of phenol. *Appl. Catal. B Environ.* 204, 566–576. <https://doi.org/10.1016/j.apcatb.2016.12.005>.
- Ghaedi, M. et al, 2018. Removal of methylene blue by silver nanoparticles loaded on activated carbon by an ultrasound-assisted device: optimization by experimental design methodology. *Res. Chem. Intermed.* 44 (5), 2929–2950. <https://doi.org/10.1007/s11164-015-2285-x>.
- Ghaziaskar, A., McRae, G.A., MacKintosh, A., Basu, O.D., 2019. Catalyzed hydrothermal carbonization with process liquid recycling. *Energy and Fuels* 33 (2), 1167–1174. <https://doi.org/10.1021/acs.energyfuels.8b03454>.
- González-Arias, J. et al, 2020. Hydrothermal carbonization of olive tree pruning as a sustainable way for improving biomass energy potential: effect of reaction parameters on fuel properties. *Processes* 8 (10), 1201. <https://doi.org/10.3390/PR8101201>.
- P. Goos and B. Jones, *Optimal Design of Experiments: A Case Study Approach*. 2011. doi: 10.1002/9781119974017.
- M. Grifoni, F. Pedron, M. Barbaferi, I. Rosellini, G. Petruzzelli, and E. Franchi, “Sustainable Valorization of Biomass: From Assisted Phytoremediation to Green Energy Production,” in *Handbook of Assisted and Amendment: Enhanced Sustainable Remediation Technology*, John Wiley & Sons, Ltd, 2021, pp. 29–51. doi: 10.1002/9781119670391.ch2
- Hameed, B.H., El-Khaiary, M.I., 2008. Malachite green adsorption by rattan sawdust: Isotherm, kinetic and mechanism modeling. *J. Hazard. Mater.* 159 (2–3), 574–579. <https://doi.org/10.1016/j.jhazmat.2008.02.054>.
- Heidari, M., Dutta, A., Acharya, B., Mahmud, S., 2019. A review of the current knowledge and challenges of hydrothermal carbonization for biomass conversion. *J. Energy Inst.* 92 (6), 1779–1799. <https://doi.org/10.1016/j.joei.2018.12.003>.
- M. Heidari, O. Norouzi, S. Salaudeen, B. Acharya, and A. Dutta, *Prediction of Hydrothermal Carbonization with Respect to the Biomass Components and Severity Factor*, vol. 33, no. 10. 2019. doi: 10.1021/acs.energyfuels.9b02291
- Hsini, N., Abdelwaheb, M., Dhaouadi, H., Dridi-Dhaouadi, S., 2020. Valorization of solid wastes from Ditttrichia essential oil extraction as biosorbents for cadmium removal: biosorbent characterizations and isotherm modeling. *Int. J. Environ. Sci. Technol.* 17 (11), 4611–4622. <https://doi.org/10.1007/s13762-020-02803-z>.
- Huh, S.H., 2014. X-ray diffraction of multi-layer graphenes: Instant measurement and determination of the number of layers. *Carbon* N. Y. 78, 617–621. <https://doi.org/10.1016/j.carbon.2014.07.034>.
- A. Jain, R. Balasubramanian, and M. P. Srinivasan, “Hydrothermal conversion of biomass waste to activated carbon with high porosity: A review,” *Chemical Engineering Journal*, vol. 283. Elsevier B.V., pp. 789–805, 2016. doi: 10.1016/j.cej.2015.08.014.
- W. Ke, “The Optimal Design of Blocked and Split-Plot Experiments,” *Technometrics*, vol. 47, no. 1, pp. 94–94, 2005, doi: 10.1198/tech.2005.s822.
- P. Klobes, K. Meyer, and R. G. Munro, “Porosity and Specific Surface Area Measurements for Solid Materials,” *Mater. Sci.*, vol. 960–17, p. 79, 2006, [Online]. Available: <http://www.ncbi.nlm.nih.gov/pubmed/22544181>
- Kumar, A., Jena, H.M., 2016. Preparation and characterization of high surface area activated carbon from Fox nut (*Euryale ferox*)

- shell by chemical activation with H₃PO₄. *Results Phys.* 6, 651–658. <https://doi.org/10.1016/j.rinp.2016.09.012>.
- Kurnia, K.A. et al, 2022. Insight into the adsorption of dyes onto chitin in aqueous solution: an experimental and computational study. *Arab. J. Chem.* 15, (11). <https://doi.org/10.1016/j.arabjc.2022.104293> 104293.
- Li, X. et al, Jul. 2022. Conversion of Lavandula straw into high-quality solid fuel: effect of hydrothermal carbonization conditions on fuel characteristics. *Bioenergy Res.*, 1–17 <https://doi.org/10.1007/s12155-022-10492-4>.
- Liu, D. et al, 2020. Preparation of highly porous graphitic activated carbon as electrode materials for supercapacitors by hydrothermal pretreatment-assisted chemical activation. *ACS Omega* 5 (19), 11058–11067. <https://doi.org/10.1021/acsomega.0c00938>.
- Liu, Z., Balasubramanian, R., 2012. Hydrothermal carbonization of waste biomass for energy generation. *Procedia Environ. Sci.* 16, 159–166. <https://doi.org/10.1016/j.proenv.2012.10.022>.
- D. Liu et al., “Microwave-Assisted Hydrothermal Preparation of Corn Straw Hydrochar as Supercapacitor Electrode Materials,” 2020, doi: 10.1021/acsomega.0c03605
- Lopes, G.K.P. et al, 2021. Steam-activated carbon from malt bagasse: optimization of preparation conditions and adsorption studies of sunset yellow food dye. *Arab. J. Chem.* 14, (3). <https://doi.org/10.1016/j.arabjc.2021.103001> 103001.
- K. MacDermid-Watts, R. Pradhan, and A. Dutta, “Catalytic Hydrothermal Carbonization Treatment of Biomass for Enhanced Activated Carbon: A Review,” *Waste and Biomass Valorization*, no. 0123456789, 2020, doi: 10.1007/s12649-020-01134-x
- Magdy, Y.H., Altaher, H., 2018. Kinetic analysis of the adsorption of dyes from high strength wastewater on cement kiln dust. *J. Environ. Chem. Eng.* 6 (1), 834–841. <https://doi.org/10.1016/j.jece.2018.01.009>.
- Masinga, T., Moyo, M., Pakade, V.E., 2022. Removal of hexavalent chromium by polyethyleneimine impregnated activated carbon: intra-particle diffusion, kinetics and isotherms. *J. Mater. Res. Technol.* 18, 1333–1344. <https://doi.org/10.1016/j.jmrt.2022.03.062>.
- McKay, G., Otterburn, M.S., Aga, J.A., 1987. Intraparticle diffusion process occurring during adsorption of dyestuffs. *Water. Air. Soil Pollut.* 36 (3–4), 381–390. <https://doi.org/10.1007/BF00229680>.
- Nhuchhen, D.R., Afzal, M.T., 2017. HHV predicting correlations for torrefied biomass using proximate and ultimate analyses. *Bioengineering* 4 (1), pp. <https://doi.org/10.3390/bioengineering4010007>.
- Nizamuddin, S. et al, 2017. An overview of effect of process parameters on hydrothermal carbonization of biomass. *Renew. Sustain. Energy Rev.* 73 (February), 1289–1299. <https://doi.org/10.1016/j.rser.2016.12.122>.
- J. Nocedal and S. J. Wright, “Numerical optimization,” in *Springer Series in Operations Research and Financial Engineering*, 2006, pp. 1–664. doi: 10.1201/b19115-11
- Oginni, O., Singh, K., Oporto, G., Dawson-Andoh, B., McDonald, L., Sabolsky, E., 2019. Influence of one-step and two-step KOH activation on activated carbon characteristics. *Bioresour. Technol. Reports* 7, <https://doi.org/10.1016/J.BITEB.2019.100266> 100266.
- J. A. Okolie et al., “Waste biomass valorization for the production of biofuels and value-added products: A comprehensive review of thermochemical, biological and integrated processes,” *Process Safety and Environmental Protection*, vol. 159. Elsevier, pp. 323–344, Mar. 01, 2022. doi: 10.1016/j.psep.2021.12.049.
- S. Oumabady, P. S. Paul Sebastian, S. P. B. Kamaludeen, M. Ramasamy, P. Kalaiselvi, and E. Parameswari, “Preparation and Characterization of Optimized Hydrochar from Paper Board Mill Sludge,” *Sci. Rep.*, vol. 10, no. 1, p. 773, Dec. 2020, doi: 10.1038/s41598-019-57163-7.
- Pavlović, I., Knez, Ž., Škerget, M., 2013. Hydrothermal reactions of agricultural and food processing wastes in sub- and supercritical water: a review of fundamentals, mechanisms, and state of research. *J. Agric. Food Chem.* 61 (34), 8003–8025. <https://doi.org/10.1021/jf401008a>.
- Politis, S.N., Colombo, P., Colombo, G., Rekkas, D.M., 2017. Design of experiments (DoE) in pharmaceutical development. *Drug Dev. Ind. Pharm.* 43 (6), 889–901. <https://doi.org/10.1080/03639045.2017.1291672>.
- F. Pukelsheim, *Optimal Design of Experiments*, Classic Ed. Society for Industrial and Applied Mathematic, 2006. doi: 10.1137/1.9780898719109.
- Rather, M.A., Khan, N.S., Gupta, R., 2017. Catalytic hydrothermal carbonization of invasive macrophyte Hornwort (*Ceratophyllum demersum*) for production of hydrochar: a potential biofuel. *Int. J. Environ. Sci. Technol.* 14 (6), 1243–1252. <https://doi.org/10.1007/s13762-016-1227-5>.
- Rodríguez Correa, C., Ngamyng, C., Klank, D., Kruse, A., 2018. Investigation of the textural and adsorption properties of activated carbon from HTC and pyrolysis carbonizates. *Biomass Convers. Biorefinery* 8 (2), 317–328. <https://doi.org/10.1007/s13399-017-0280-8>.
- Román, S., Nabais, J.M.V., Laginhas, C., Ledesma, B., González, J. F., 2012. Hydrothermal carbonization as an effective way of densifying the energy content of biomass. *Fuel Process. Technol.* 103, 78–83. <https://doi.org/10.1016/J.FUPROC.2011.11.009>.
- P. K. Rout, A. D. Nannaware, and R. Rajasekharan, “PROCESS FOR CHEMICAL CONVERSION OF CELLULOSE SOLATED FROM AROMATIC SPENT BOMASS TO HYDROXYMETHYL FURFURAL,” 2015 Accessed: Nov. 23, 2022. [Online]. Available: <https://patents.google.com/patent/US9199956B2/en>.
- A. Saha and B. B. Basak, “Scope of value addition and utilization of residual biomass from medicinal and aromatic plants,” *Industrial Crops and Products*, vol. 145. Elsevier, p. 111979, Mar. 01, 2020. doi: 10.1016/j.indcrop.2019.111979.
- A. salah omer et al., “Adsorption of crystal violet and methylene blue dyes using a cellulose-based adsorbent from sugercane bagasse: characterization, kinetic and isotherm studies,” *J. Mater. Res. Technol.*, vol. 19, pp. 3241–3254, Jul. 2022, doi: 10.1016/j.jmrt.2022.06.045.
- O. Santana-Méridas, A. González-Coloma, and R. Sánchez-Vioque, “Agricultural residues as a source of bioactive natural products,” *Phytochemistry Reviews*, vol. 11, no. 4. Springer, pp. 447–466, Nov. 30, 2012. doi: 10.1007/s11101-012-9266-0.
- Scherrer, P., 1918. Bestimmung der inneren Struktur und der Größe von Kolloidteilchen mittels Röntgenstrahlen. *Kolloidchemie Ein Lehrbuch* 1912, 387–409. https://doi.org/10.1007/978-3-662-33915-2_7.
- Sekine, T., Nakatani, K., 2002. Intraparticle diffusion and adsorption isotherm for sorption in silica gel studied by single-microparticle injection and microabsorption methods. *Langmuir* 18 (3), 694–697. <https://doi.org/10.1021/la0110500>.
- Sepehrnia, M., Farrokh, M.J., Karimi, M., Mohammadzadeh, K., 2023. Experimental study and development of mathematical model using surface response method to predict the rheological performance of CeO₂-CuO/10W40 hybrid nanolubricant. *Arab. J. Chem.* 16, (6). <https://doi.org/10.1016/j.arabjc.2023.104721> 104721.
- A. Slavov, I. Vasileva, L. Stefanov, and A. Stoyanova, “Valorization of wastes from the rose oil industry,” *Reviews in Environmental Science and Biotechnology*, vol. 16, no. 2. Springer, pp. 309–325, Apr. 22, 2017. doi: 10.1007/s11157-017-9430-5.
- B. Smucker, M. Krzywinski, and N. Altman, “Optimal experimental design,” *Nature Methods*, vol. 15, no. 8. Nature Publishing Group, pp. 559–560, Aug. 01, 2018. doi: 10.1038/s41592-018-0083-2.
- Supong, A., Sinha, U.B., Sinha, D., 2022. Density functional theory calculations of the effect of oxygenated functionals on activated carbon towards cresol adsorption. *Surfaces* 5 (2), 280–289. <https://doi.org/10.3390/surfaces5020020>.
- Susanti, R.F., Arie, A.A., Kristianto, H., Erico, M., Kevin, G., Devianto, H., 2019. Activated carbon from citric acid catalyzed hydrothermal carbonization and chemical activation of salacca peel as potential electrode for lithium ion capacitor’s cathode. *Ionics*

- (Kiel) 25 (8), 3915–3925. <https://doi.org/10.1007/s11581-019-02904-x>.
- Susanti, R.F., Wiratmadja, R.G.R., Kristianto, H., Arie, A.A., Nugroho, A., 2022. Synthesis of high surface area activated carbon derived from cocoa pods husk by hydrothermal carbonization and chemical activation using zinc chloride as activating agent. *Mater. Today Proc.* 63, S55–S60. <https://doi.org/10.1016/j.matpr.2022.01.042>.
- Theydan, S.K., Ahmed, M.J., 2012. Adsorption of methylene blue onto biomass-based activated carbon by FeCl₃ activation: equilibrium, kinetics, and thermodynamic studies. *J. Anal. Appl. Pyrolysis* 97, 116–122. <https://doi.org/10.1016/j.jaap.2012.05.008>.
- Thommes, M. et al, 2015. Physisorption of gases, with special reference to the evaluation of surface area and pore size distribution (IUPAC Technical Report). *Pure Appl. Chem.* 87 (9–10), 1051–1069. <https://doi.org/10.1515/pac-2014-1117>.
- Titirici, M.M., Antonietti, M., 2010. Chemistry and materials options of sustainable carbon materials made by hydrothermal carbonization. *Chem. Soc. Rev.* 39 (1), 103–116. <https://doi.org/10.1039/b819318p>.
- Tu, W. et al, 2021. A novel activation-hydrochar via hydrothermal carbonization and KOH activation of sewage sludge and coconut shell for biomass wastes: preparation, characterization and adsorption properties. *J. Colloid Interface Sci.* 593, 390–407. <https://doi.org/10.1016/j.jcis.2021.02.133>.
- Tunç, I.D., Erol, M., Güneş, F., Sütçü, M., 2020. Growth of ZnO nanowires on carbon fibers for photocatalytic degradation of methylene blue aqueous solutions: an investigation on the optimization of processing parameters through response surface methodology/central composite design. *Ceram. Int.* 46 (6), 7459–7474. <https://doi.org/10.1016/j.ceramint.2019.11.244>.
- V. Vadivelan and K. Vasanth Kumar, “Equilibrium, kinetics, mechanism, and process design for the sorption of methylene blue onto rice husk,” *J. Colloid Interface Sci.*, vol. 286, no. 1, pp. 90–100, Jun. 2005, doi: 10.1016/j.jcis.2005.01.007.
- Veloso, C.H., Filippov, L.O., Filippova, I.V., Ouvrard, S., Araujo, A. C., 2020. Adsorption of polymers onto iron oxides: equilibrium isotherms. *J. Mater. Res. Technol.* 9 (1), 779–788. <https://doi.org/10.1016/j.jmrt.2019.11.018>.
- Vinayagam, R. et al, 2023. Bioinspiration synthesis of hydroxyapatite nanoparticles using eggshells as a calcium source: evaluation of Congo red dye adsorption potential. *J. Mater. Res. Technol.* 22, 169–180. <https://doi.org/10.1016/J.JMRT.2022.11.093>.
- Weissman, S.A., Anderson, N.G., 2015. Design of experiments (DoE) and process optimization. a review of recent publications. *Org. Process Res. Dev.* 19 (11), 1605–1633. <https://doi.org/10.1021/op500169m>.
- X. Xing, W. Jiang, S. Li, X. Zhang, and W. Wang, “Preparation and analysis of straw activated carbon synergetic catalyzed by ZnCl₂ - H₃PO₄ through hydrothermal carbonization combined with ultrasonic assisted immersion pyrolysis,” *Waste Manag.*, vol. 89, no. x, pp. 64–72, 2019, doi: 10.1016/j.wasman.2019.04.002
- Xue, Y. et al, 2012. Hydrogen peroxide modification enhances the ability of biochar (hydrochar) produced from hydrothermal carbonization of peanut hull to remove aqueous heavy metals: Batch and column tests. *Chem. Eng. J.* 200–202, 673–680. <https://doi.org/10.1016/j.cej.2012.06.116>.
- Yao, C., Chen, T., 2017. A film-diffusion-based adsorption kinetic equation and its application. *Chem. Eng. Res. Des.* 119, 87–92. <https://doi.org/10.1016/j.cherd.2017.01.004>.
- Yao, Z., Ma, X., Lin, Y., 2016. Effects of hydrothermal treatment temperature and residence time on characteristics and combustion behaviors of green waste. *Appl. Therm. Eng.* 104, 678–686. <https://doi.org/10.1016/j.applthermaleng.2016.05.111>.
- Yusop, M.F.M., Ahmad, M.A., Rosli, N.A., Manaf, M.E.A., 2021. Adsorption of cationic methylene blue dye using microwave-assisted activated carbon derived from acacia wood: Optimization and batch studies. *Arab. J. Chem.* 14, (6). <https://doi.org/10.1016/J.ARABJC.2021.103122> 103122.
- Zbair, M. et al, 2020. Hydrothermal carbonization of Argan nut shell: functional mesoporous carbon with excellent performance in the adsorption of bisphenol A and Diuron. *Waste Biomass Valorization* 11 (4), 1565–1584. <https://doi.org/10.1007/S12649-018-00554-0/TABLES/5>.
- Zhang, S. et al, 2021. Bamboo derived hydrochar microspheres fabricated by acid-assisted hydrothermal carbonization. *Chemosphere* 263,. <https://doi.org/10.1016/j.chemosphere.2020.128093> 128093.
- Zhou, F. et al, 2022. Efficient removal of methylene blue by activated hydrochar prepared by hydrothermal carbonization and NaOH activation of sugarcane bagasse and phosphoric acid. *RSC Adv.* 12 (3), 1885–1896. <https://doi.org/10.1039/d1ra08325b>.